

1  
2  
3  
4  
5  
6  
7  
8  
9  
10  
11  
12  
13  
14  
15  
16  
17  
18  
19

REVISION 1

American Mineralogist Manuscript 6268

**A Mössbauer-based XANES calibration for hydrous basalt glasses reveals  
radiation-induced oxidation of Fe**

ELIZABETH COTTRELL<sup>1,\*</sup>, ANTONIO LANZIROTTI<sup>2</sup>, BJORN MYSEN<sup>3</sup>, SUZANNE BIRNER<sup>1,4</sup>,  
KATHERINE A. KELLEY<sup>5</sup>, ROMAN BOTCHARNIKOV<sup>6,7</sup>, FREDRICK A. DAVIS<sup>1,8</sup>, MATTHEW  
NEWVILLE<sup>2</sup>

<sup>1</sup>NMNH, Smithsonian Inst., Washington, DC 20560 USA

(\*correspondence: cottrelle@si.edu)

<sup>2</sup>University of Chicago, Chicago, IL 60637 USA

<sup>3</sup>Geophys. Lab., Carnegie Inst. Washington, DC 20015 USA

<sup>4</sup>Dept. Geol. Sci., Stanford Univ., Stanford, CA 94305 USA

<sup>5</sup>GSO, Univ. of Rhode Island, Narragansett, RI 20882 USA

<sup>6</sup>Inst. Mineralogie, Leibniz Univ. Hannover, D-30167 GE

<sup>7</sup>Inst. Geowiss., Gutenberg Univ. Mainz, D-55128 GE

<sup>8</sup>DEES, Univ. of Minnesota Duluth, Duluth, MN 55812 USA

**ABSTRACT**

Oxygen fugacity ( $fO_2$ ) exerts first-order control on the geochemical evolution of planetary interiors, crusts, and hydrospheres, and the  $Fe^{3+}/\Sigma Fe$  ratios of silicate glasses provide a useful proxy for  $fO_2$ . Fe K-edge micro X-ray Absorption Near-Edge Structure (XANES) spectroscopy allows researchers to micro-analytically determine the  $Fe^{3+}/\Sigma Fe$

25 ratios of silicate glasses with high precision. In this study we characterize hydrous and  
26 anhydrous basalt glass standards with Mössbauer and XANES spectroscopy and show  
27 that synchrotron radiation causes progressive changes to the XANES spectra of hydrous  
28 glasses as a function of radiation dose (here defined as total photons delivered per square  
29 micron), water concentration, and initial  $\text{Fe}^{3+}/\Sigma\text{Fe}$  ratio.

30

31 We report experiments from 8 different radiation dose conditions and show that Fe in  
32 hydrous silicate glasses can undergo rapid oxidation upon exposure to radiation. The rate  
33 and degree of oxidation correlates with radiation dose and the product of water  
34 concentration and ferrous/ferric iron oxide ratio on a molar basis  
35 ( $\Phi = \text{XHO}_{1.5} * \text{XFeO}/\text{XFeO}_{1.5}$ ). For example, a basalt glass with 4.9 wt.% dissolved  $\text{H}_2\text{O}$   
36 and  $\text{Fe}^{3+}/\Sigma\text{Fe} = 0.19$  from its Mössbauer spectrum may appear to have a  $\text{Fe}^{3+}/\Sigma\text{Fe} \geq 0.35$   
37 when analysed over several minutes at a nominal flux density of  $\sim 2 \times 10^9$  photons/sec/ $\mu\text{m}^2$ .  
38 This radiation-induced increase in  $\text{Fe}^{3+}/\Sigma\text{Fe}$  ratio would lead to an overestimation of  $f\text{O}_2$   
39 by  $\sim 2$  orders of magnitude, with dramatic consequences for the interpretation of  
40 geological processes.

41

42 The sample area exposed to radiation shows measureable hydrogen loss, consistent with  
43 radiation-induced breaking of O—H bonds, associated H migration and loss, and  
44 oxidation of  $\text{Fe}^{2+}$ . This mechanism is consistent with the observation that anhydrous  
45 glasses show no damage under any beam conditions. Cryogenic cooling does not  
46 mitigate, but rather accelerates, iron oxidation. The effects of beam damage appear to  
47 persist indefinitely.

48

49 We detect beam damage at the lowest photon flux densities tested ( $3 \times 10^6$   
50 photons/sec/ $\mu\text{m}^2$ ); however, at flux densities  $\leq 6 \times 10^7$  photons/sec/ $\mu\text{m}^2$ , the hydrous glass  
51 calibration curve defined by the centroid (derived from XANES spectra) and  $\text{Fe}^{3+}/\Sigma\text{Fe}$   
52 ratios (derived from Mössbauer spectra), is indistinguishable from the anhydrous  
53 calibration curve within the accuracy achievable with Mössbauer spectroscopy. Thus,  
54 published  $\text{Fe}^{3+}/\Sigma\text{Fe}$  ratios from hydrous glasses measured at low photon flux densities are  
55 likely to be accurate within measurement uncertainty with respect to what would have  
56 been measured by Mössbauer spectroscopy.

57

58 These new results demonstrate that to obtain accurate  $\text{Fe}^{3+}/\Sigma\text{Fe}$  ratios from hydrous,  
59 mafic, silicate glasses, it is first necessary to carefully monitor changes in the XANES  
60 spectra as a function of incident dose (e.g., fixed-energy scan). Defocusing and  
61 attenuating the beam may prevent significant oxidation of Fe in mafic water-bearing  
62 glasses.

63

## 64 **INTRODUCTION**

65 The  $\text{Fe}^{3+}/\Sigma\text{Fe}$  ratio of silicate glass may serve as a direct proxy for the oxygen fugacity  
66 ( $f\text{O}_2$ ) of an igneous system and exerts control on phase equilibria, physical properties, and  
67 the valence state of other heterovalent elements in solution (e.g. Carmichael, 1991; Kress  
68 and Carmichael, 1991; Sack et al., 1980). The use of Fe-K-edge XANES to obtain  
69  $\text{Fe}^{3+}/\Sigma\text{Fe}$  ratios of hydrous silicate glasses has proliferated in recent years owing to the  
70 outstanding precision achievable and micron-scale spatial resolution afforded (e.g.

71 Botcharnikov et al., 2005; Brounce et al., 2014a; Cottrell and Kelley, 2011; Gaetani et al.,  
72 2012; Helz et al., 2017; Kelley and Cottrell, 2009; Kelley and Cottrell, 2012; Le Voyer et  
73 al., 2015; Matjuschkin et al., 2015; Moor et al., 2013; Moussallam et al., 2014; Shorttle et  
74 al., 2015; Stamper et al., 2014; Wilke et al., 2006). Most Fe-XANES calibration studies  
75 have focused on anhydrous glasses, in large part because  $fO_2$  can be easily controlled in  
76 1-atmosphere gas-mixing furnaces (Berry et al., 2003; Cottrell et al., 2009; Dyar et al.,  
77 2016; Fiege et al., 2017; Wilke et al., 2001; Wilke et al., 2005; Zhang et al., submitted;  
78 Zhang et al., 2016). Given the recent surge in Fe-XANES-based research, however, it is  
79 important to understand and quantify how dissolved water and radiation-induced  
80 chemical reactions may modify the spectral features used to determine  $Fe^{3+}/\Sigma Fe$  ratios.  
81  
82 Fe-XANES pre-edge features are sensitive to the coordination environment and oxidation  
83 state of Fe (e.g. Henderson et al., 2014 and references therein). The potential effects of  
84 water dissolved in silicate glass on the structural environment of Fe are therefore of great  
85 interest to practitioners of XANES. In their Mössbauer studies on glasses, Wilke et al.  
86 (2002, 2006) observed differences in the hyperfine fields and coordination environments  
87 between hydrous and anhydrous glasses, but postulated that the differences emerged  
88 during quench. Wilke and co-workers concluded that there is no detectable influence of  
89 water on the local structural environment of Fe in melts. The effect of dissolved water on  
90 the oxidation state of Fe in melts has been the subject of more study and debate, but  
91 XANES and wet-chemical studies of mafic glasses synthesized at fixed  $fO_2$  have shown  
92 water to have no effect on  $Fe^{3+}/\Sigma Fe$  ratios (Botcharnikov et al., 2005; Gaillard et al.,  
93 2001; Moore et al., 1995). Given that Fe coordination affects pre-edge intensities, but not

94 the pre-edge centroids most commonly employed to extract  $\text{Fe}^{3+}/\Sigma\text{Fe}$  ratios (Bajt et al.,  
95 1994; Cottrell et al., 2009; Wilke et al., 2005), and the difficulty of independently varying  
96  $f\text{O}_2$  and  $f\text{H}_2\text{O}$  in experimental systems, relatively little effort has been applied to  
97 calibrating hydrous glasses for XANES determinations of  $\text{Fe}^{3+}/\Sigma\text{Fe}$  ratios.

98

99 Electron and X-ray beam interactions with materials can shift the oxidation state of  
100 various elements in biological, amorphous, and crystalline materials (e.g. Corbett et al.,  
101 2007; Eeckhout et al., 2005; Shimizugawa et al., 2001; Gonçalves Ferreira et al., 2013).  
102 For example, sulfur dissolved in silicate glass may become oxidized or reduced upon  
103 exposure to electron and X-ray beams (Klimm et al., 2012; Rowe et al., 2007; Wilke et  
104 al., 2008). Relatively little work has been done to investigate the potential effects of  
105 radiation on Fe speciation in silicate glasses. Wilke et al. (2005) and Cottrell et al. (2009)  
106 assessed, but saw no evidence for, radiation-induced beam damage in XANES spectra of  
107 anhydrous basalt glasses collected at bending magnet sources. Shorttle et al. (2015)  
108 assessed beam damage in glasses with <1 wt.% water, and observed an increase in the  
109 intensity of the second pre-edge multiplet with time (radiation dose) using an  
110 unattenuated undulator-source that was “barely above instrument stability” (i.e. was  
111 within the noise). The study of Moussallam et al. (2016) was not able to detect beam  
112 damage by analyzing successive XANES spectra collected at a single spot on glasses  
113 with <1 wt.% water at an attenuated undulator-source. However, as new radiation sources  
114 come online that can deliver higher flux densities to a sample, and studies of hydrous  
115 silicate glass proliferate, we find it prudent to examine the potential for radiation to  
116 induce beam damage.

117

118 **SAMPLES AND METHODS**

119 *Samples.* We examine 27 glasses of basaltic composition in this study: 13 anhydrous  
120 basalt glasses from the study of (Cottrell et al., 2009), which are available to the  
121 community upon request to Smithsonian's National Rock Collection, and 14 hydrous  
122 glasses (0.72 to 4.82 wt.% dissolved total H<sub>2</sub>O) from the study of (Botcharnikov et al.,  
123 2005). For this study, all analyses were performed on double-side polished glass wafers  
124 of approximately 50-100µm in thickness. Details of the experimental methods and  
125 complete sample characterizations can be found in Cottrell et al. (2009), Cottrell and  
126 Kelley (2011) (including wet-chemical analyses), and Botcharnikov et al. (2005).

127

128 *Analytical Methods.*

129 *Mössbauer Spectroscopy.* Cottrell et al. (2009) and Botcharnikov et al. (2005) report  
130 Fe<sup>3+</sup>/ΣFe ratios for each glass based on room temperature Mössbauer spectroscopy,  
131 without correction for recoilless fraction. We re-report their results in Table 1, along with  
132 new fits to the hydrous B glasses discussed below. Method details for previously reported  
133 fits can be found in Cottrell et al. (2009) and Botcharnikov et al. (2005). Cottrell et al.  
134 (2009) applied the distribution fitting method of Alberto et al. (1996), which adopts a  
135 two-dimensional (2D) Gaussian probability distribution function for the isomer shift and  
136 quadrupole splitting. This routine minimizes the error (reduced  $\chi^2$  values) between the  
137 data and the absorption envelope that arises from the contribution of paramagnetic  
138 quadrupole doublets. The area of the fitted ferric doublet relative to the entire absorption  
139 envelope provides the Fe<sup>3+</sup>/ΣFe ratio. Using the software package RECOIL (Lagarec and

140 Rancourt, 1998), Botcharnikov et al. (2005) applied an extended Voigt-based fitting  
141 (xVBF) method that also assumes a two-dimensional Gaussian distribution of hyperfine  
142 parameters for ferric and ferrous iron (Lagarec and Rancourt, 1997). The relative area  
143 ratios provide the  $\text{Fe}^{3+}/\Sigma\text{Fe}$  ratios, and the uncertainties estimated by Botcharnikov et al.  
144 (2005) that we re-report in Table 1 reflect counting statistics, variation in the results from  
145 the application of multiple fitting models, and the possible effect of neglecting the  
146 recoilless fraction.

147

148 To isolate the effects of beam damage, deconvolution of the Mössbauer spectra for  
149 hydrous and anhydrous glasses must be consistent. Both xVBF and Alberto et al. (1996)  
150 methods fit multiple distributions (based on a Gaussian distribution of Lorentzian line  
151 shapes). The site distributions derive from maxima in the probability functions that  
152 describe the ferrous and ferric hyperfine field distributions (Mysen et al., 2006, and  
153 references therein). Zhang et al. (submitted) show that both approaches yield consistent  
154  $\text{Fe}^{3+}/\Sigma\text{Fe}$  ratios for the AII and LW glasses. To test for systematic bias between the  
155 Cottrell et al. (2009) and Botcharnikov et al. (2005) approaches, we obtained the raw  
156 spectra of Botcharnikov et al. (2005), collected at Bayerisches Geoinstitute, University of  
157 Bayreuth, and refit 14 of them using the same methods used by Cottrell et al. (2009). This  
158 ensures that our analysis of oxidative beam damage from synchrotron radiation will not  
159 be affected by inter-laboratory bias in the Mössbauer fitting protocols.

160

161 *X-ray Absorption Near Edge Structure (XANES) Spectroscopy*. Cottrell et al. (2009) and  
162 Botcharnikov et al. (2005) report on Fe K-edge XANES spectra collected previously for

163 the glasses used in this study. The former collected spectra at the bending magnet station  
164 X26A at the National Synchrotron Light Source (NSLS), Brookhaven National  
165 Laboratory, New York, USA, and the latter at the Hamburger  
166 Synchrotronstrahlungslabor (HASYLAB), Hamburg, GE. Details about those facilities,  
167 collection procedures, and fitting routines can be found in Cottrell et al. (2009) and  
168 Botcharnikov et al. (2005).

169

170 For this study, we collected new Fe K-edge XANES spectra on the AII, LW, and B series  
171 glasses in fluorescence mode in six synchrotron beam sessions: two on bending magnet  
172 station X26A at NSLS in 2015, and four at station 13-ID-E (GSECARS) at the Advanced  
173 Photon Source (APS), Argonne National Laboratory, IL, USA, in 2014 - 2016. We  
174 applied 8 radiation dose conditions that we detail in Table 2. We cast our results in terms  
175 of radiation dose so that the results can be easily generalized to other facilities and  
176 beamline configurations. For these experiments it is more convenient and descriptive to  
177 represent the mean energy imparted to the sample in terms of flux density, rather than in  
178 the more standard SI units of Gray. However, the absorbed dose in Gray (absorption of  
179 one joule of radiation energy per kilogram of sample) can be calculated by assuming an  
180 average basaltic glass composition and density and the depth at which the incident  
181 radiation falls to 1/e within the glass (Henke et al. 1993). For basaltic glass, the flux  
182 density is equivalent to ~75-80 times the dose in Grays/sec (Table 2). As we describe  
183 below, in all sessions, and at all facilities, we set the area-weighted average energy of the  
184 pre-edge peaks (the centroid) equal to 7112.3 for anhydrous glass standard LW\_0  
185 (Cottrell et al., 2009). LW\_0 is analysed frequently throughout all analytical sessions.

186 Normalization of all centroids to the energy drift-corrected centroid of LW\_0 accounts  
187 for within-session instrumental drift in the monochromator energy calibration and for  
188 differences in monochromator calibration between facilities and between sessions (Bajt et  
189 al., 1994; Cottrell et al., 2009). The empirical drift-corrected precision ( $1\sigma$ ) of the area-  
190 weighted centroid positions collected over a ten-year period on the AII and LW glasses is  
191  $0.004\pm 0.009$  eV (n for each glass = 30-50) (Zhang et al., submitted).

192

193 We did not correct for over-absorption effects (Manceau et al., 2002). In fluorescence  
194 mode XANES, over-absorption can result in a decrease in the amplitude of the absorption  
195 peaks in samples where the absorber mass is high. This can result in a relative increase in  
196 the pre-edge peak intensities relative to the main absorption edge, but it does not impact  
197 the relative intensities of the two pre-edge peak multiplets or their energy positions  
198 (Botcharnikov et al., 2005; Cottrell et al., 2009; Zhang et al., 2016). Moreover, while  
199 over-absorption can affect pre-edge peak intensities, all glass compositions examined  
200 here have sufficiently high total FeO contents (7-12 wt.%) and thicknesses ( $> 50\mu\text{m}$ ) to  
201 be in the infinite thickness regime.

202

203 *X26A, NSLS, Brookhaven National Laboratory, USA*. NSLS (decommissioned in  
204 October, 2014) operated at 2.8 GeV and 300 mA. We collected fluorescence spectra on  
205 the B series glasses at bending magnet beamline X26A using summed energy dispersive  
206 spectra from a 4-element Vortex ME-4 silicon drift diode detector and two single element  
207 Vortex-EX detectors (Hitachi) with pulse processing provided by an XMap digital  
208 spectrometer system (XIA). The first derivative of Fe K-edge spectra ( $E_0$ ) collected on

209 zero-valent Fe  $E_0$  is 7112.0 eV. All other methods details are as reported by Cottrell et al.  
210 (2009). The incident beam flux at X26A was consistently  $\sim 3 \times 10^9$  photons/sec and the  
211 spot size was 9 x 5 microns such that the photon flux density was  $\sim 6.7 \times 10^7$   
212 photons/sec/ $\mu\text{m}^2$  (Table 2); after a 15.5 minute collection the absorbed dose per spectrum  
213 was  $\sim 6 \times 10^{10}$  photons/ $\mu\text{m}^2$ .

214

215 *13-ID-E, GSECARS, Advanced Photon Source, Argonne National Laboratory, USA.*

216 Details regarding the beamline configuration for 13-ID-E can be found in Sutton et al.  
217 (2017). This undulator-based beam line at APS operates at 7 GeV and 85-101 mA. We  
218 collected fluorescence spectra with a Vortex ME4 silicon-drift diode detector array  
219 coupled to a high-speed digital spectrometer system (Quantum Xpress3). A cryogenically  
220 cooled double-crystal Si (311) monochromator provided the monochromatic radiation.  
221 The first derivative of Fe K-edge spectra ( $E_0$ ) collected on zero-valent Fe  $E_0$  is 7110.75  
222 eV. We collected spectra from 7012 to 7102 eV in 2.5 eV steps with 1 sec dwell; from  
223 7102 to 7132 eV (pre-edge region) in 0.1 eV steps with 1 sec dwell and from 7132 to  
224 7492 eV (XAFS region) in 2.3 angstrom steps with 1 sec dwell. We edge-step normalized  
225 the spectra collected at 13-ID-E by the average intensity between 7315 and 7320 eV  
226 where the spectra were flat.

227

228 The 13-ID-E beamline is capable of delivering and detecting in excess of  $1 \times 10^{12}$   
229 photons/sec within a focused spot size of 2 x 2 microns at the Fe K-edge, so that focused  
230 flux densities of  $\sim 5 \times 10^{11}$  photons/sec/ $\mu\text{m}^2$  are possible – four orders of magnitude higher  
231 than what was possible at X26A. We collected the experimental data presented here over

232 a  $\sim 10^4$  range in flux density to precisely assess the spectral response to absorbed radiation  
233 dose. At 13-ID-E we collected spectra using 6 protocols where incident flux density was  
234 adjusted, through upstream aperturing of the X-ray beam; through filtering using varying  
235 thicknesses of aluminium foil; and through defocusing of the incident beam on the  
236 sample. These conditions are reported in Table 2.

237

238 We also conducted one set of analyses at 13-ID-E under cryogenic conditions, using a  
239 customized cryogenic stage described in Tappero et al. (2016, 2017), to investigate the  
240 degree to which cryogenic cooling may mitigate the observed iron oxidation. We  
241 collected a time series at an energy of 7113.3 eV at both ambient and cryogenic  
242 conditions reported in Table 2.

243

#### 244 *Fourier Transform Infrared (FTIR) Spectroscopy*

245 Glass chip B10 (Table 1) was analyzed by FTIR for dissolved total H<sub>2</sub>O using a Thermo  
246 Nicolet iS50 FTIR bench spectrometer coupled with a Continuum IR microscope with  
247 automated mapping capability at the Graduate School of Oceanography, University of  
248 Rhode Island. We mapped an area on a chip of B10 that had been purposely exposed to  
249 high photon flux at beamline 13-ID-E. The map was collected using transmission FTIR  
250 with a 20 x 20  $\mu\text{m}$  square aperture and no overlap between pixels. Each spectrum was  
251 collected over 1200-6000  $\text{cm}^{-1}$  wavenumbers using 256 scans at 1  $\text{cm}^{-1}$  resolution.  
252 Individual transmission spectra were reduced for H<sub>2</sub>O<sup>Total</sup> after fitting the spectral  
253 background with a spline function and calculating the net intensity of the absorbance  
254 band at 3500  $\text{cm}^{-1}$ . The H<sub>2</sub>O<sup>Total</sup> concentration was then calculated using the Beer-

255 Lambert law, a calculated density of  $2.90 \text{ g/cm}^3$ , thickness of  $49 \pm 1 \text{ }\mu\text{m}$ , and the molar  
256 absorption coefficient  $\epsilon^{3530} = 63$ , which is assumed constant within the compositional  
257 range of basalts (Dixon et al., 1995).

258

## 259 **RESULTS**

### 260 *Mössbauer Spectra*

261 Mössbauer-derived  $\text{Fe}^{3+}/\Sigma\text{Fe}$  ratios are not very sensitive to fitting philosophy or method,  
262 but in this study we re-fit the B glass spectra acquired by Botcharnikov et al. (2005) to  
263 eliminate any potential bias between the disparate fitting routines of Cottrell et al. (2009)  
264 and Botcharnikov et al. (2005). In addition, our new fits allow us to report hyperfine  
265 parameters for these glasses that may aid in understanding the structural environment of  
266 Fe in hydrous and anhydrous glasses. We provide the Mössbauer spectra from  
267 Botcharnikov et al. (2005) and our fits from this study (both raw data and plots) in the  
268 Supplementary Material.

269

270 Two quadrupole doublets, one ferric with a low IS of 0.4 to 0.6 mm/s (relative to Fe  
271 metal) and low QS of 0.8 to 1.1 mm/s, and one ferrous with a high isomer shift of 0.8 to  
272 1.0 mm/s and quadrupole splitting of 1.9 to 2.2 mm/s, describe the Mössbauer spectra of  
273 the B glasses (Table 1, and Figures S1, S2). The Botcharnikov et al. (2005) study did not  
274 report hyperfine parameters, but the hyperfine parameters derived from the glass spectra  
275 in this study are similar to those reported previously in the literature for silicate glasses  
276 (Alberto et al., 1996; Jayasuriya et al., 2004; Mysen et al., 1985a; Zhang et al., 2016).  
277 Ferrous iron IS and QS in the hydrous B glasses are within error of those for the

278 anhydrous glasses for all but the most highly oxidized glasses, for which the quadrupole  
279 splitting in the hydrous glasses is higher. The QS for ferric iron is smaller in hydrous  
280 glasses than in anhydrous glasses by approximately 0.25 to 0.45 mm/s. The IS of ferric  
281 iron is slightly higher in the hydrous glasses than in the anhydrous glasses, and decreases  
282 with increasing  $\text{Fe}^{3+}/\Sigma\text{Fe}$  ratio, as expected (Mysen and Richet, 2005; Mysen and Virgo,  
283 1989; Mysen et al., 2006). While many factors influence the coordination of ferric iron in  
284 silicate glasses (Mysen and Richet, 2005), the greater ferric IS observed in the hydrous  
285 glasses suggests that the O— $\text{Fe}^{3+}$  bond length is longer, and weaker (e.g. Johnson et al.,  
286 1999), and that ferric iron is in higher average coordination (greater domination of  $^{\text{VI}}\text{Fe}^{3+}$ )  
287 in the hydrous B glasses than in the anhydrous AII and LW glasses. Higher coordination  
288 of ferric iron in the hydrous glasses is consistent with results from (Wilke et al., 2002;  
289 Wilke et al., 2006), and is corroborated by XANES spectra, as we discuss below.

290

291 The  $\text{Fe}^{3+}/\Sigma\text{Fe}$  ratios in the B glasses, as determined by the new fits reported here, range  
292 from 0.12 to 0.56, compared to 0.10 to 0.60 for those same glasses reported in  
293 Botcharnikov et al. (2005). The  $\text{Fe}^{3+}/\Sigma\text{Fe}$  ratios of all B glasses with nominal  $\text{Fe}^{3+}/\Sigma\text{Fe}$   
294  $<0.50$  agreed within  $1\sigma$  (2.7% absolute) with the values reported by Botcharnikov et al.  
295 (2005). The three glasses with  $\text{Fe}^{3+}/\Sigma\text{Fe}$  ratios  $>0.50$  agreed within  $2\sigma$  of the  
296 uncertainties on the fits (4.4% absolute). These fits are within the commonly accepted  
297 uncertainty of the technique, which ranges from  $\pm 1$  to 6% in absolute  $\text{Fe}^{3+}/\Sigma\text{Fe}$  ratio  
298 (Dyar et al., 1987; Mysen et al., 1985a; Mysen et al., 1985b).  $\text{Fe}^{3+}/\Sigma\text{Fe}$  ratios from the  
299 Botcharnikov et al. (2005) study correlate very well with ratios obtained in this study ( $R^2$   
300  $>0.99$ ,  $m = 0.9$ ,  $b = 1.87$ ). Consistent with the results of Cottrell et al. (2009), Zhang et

301 al. (2015), and Zhang et al. (submitted), inclusion of a second doublet in the present study  
302 did not reduce the  $\chi^2$  of the fits.

303

304 *XANES*

305 *Bending Magnet Beamlines, X26A NSLS.*

306 Full XANES spectra of hydrous B and anhydrous AII and LW glasses collected at  
307 bending magnet beamline X26A are shown in Figure 1. We provide spectra for AII and  
308 LW anhydrous glasses for a 2014 NSLS session for reference (there is no substantive  
309 change since their initial publication in Cottrell et al., 2009). As demonstrated by  
310 Botcharnikov et al. (2005) for previous XANES analyses of the B glasses, the energy of  
311 the main absorption edge, the ratio of pre-edge peak intensities, and the area-weighted  
312 average energy of the pre-edge peaks (the centroid) in the XANES spectra shift smoothly  
313 as a function of  $\text{Fe}^{3+}/\Sigma\text{Fe}$  ratio (e.g., Berry et al., 2003; Botcharnikov et al., 2005; Cottrell  
314 et al., 2009; Wilke et al., 2005). The shift in centroid energy provides a precise proxy for  
315  $\text{Fe}^{3+}/\Sigma\text{Fe}$  ratio in basaltic glasses, especially for  $\text{Fe}^{3+}/\Sigma\text{Fe}$  ratios below 0.50 (Henderson et  
316 al., 2014). We report the centroids and pre-edge peak intensities for all glasses in Table 3.  
317 We provide all fitting parameters in Table S2. Consistent with the results of Cottrell et al.  
318 (2009), centroids obtained from spatially independent spectra are precise to  $\leq \pm 0.01$  eV.

319

320 For anhydrous LW and AII glasses and hydrous B glasses, we plot the  $\text{Fe}^{3+}/\Sigma\text{Fe}$  ratios  
321 derived from Mössbauer fits determined by Botcharnikov et al. (2005) and this study  
322 against the  $\text{Fe}^{3+}/\Sigma\text{Fe}$  ratios derived from XANES at low flux using the anhydrous  
323 calibration curve of Cottrell et al. (2009). Regardless of which set of Mössbauer values

324 are used, the  $\text{Fe}^{3+}/\Sigma\text{Fe}$  ratios of the hydrous glasses fall within  $1\sigma$  of a 1:1 relationship  
325 (Figure 2a).

326

327 *Undulator-based Beamlines, 13-ID-E, APS.*

328 Full XANES spectra of AII, LW, and B glasses collected at insertion device beamline 13-  
329 ID-E (GSECARS) are shown in Figure 1 and we provide fitting parameters in Table S2.

330

331 *Condition XANES<sub>1</sub>, Anhydrous Glasses.* We report centroids (area weighted average  
332 energy of the two pre-edge multiplets) under “nominal” operating conditions at 13-ID-E,  
333 our condition “XANES<sub>1</sub>,” for each glass in Table 3.

334

335 Under normal high flux operating conditions at station 13-1D-E, we recover the  $\text{Fe}^{3+}/\Sigma\text{Fe}$   
336 ratios of anhydrous glasses when we use the calibration of Cottrell et al. (2009), which  
337 was developed at low flux. Anhydrous glass  $\text{Fe}^{3+}/\Sigma\text{Fe}$  ratios derived from XANES at  
338 high flux fall within  $1\sigma$  of a 1:1 relationship with the Mossbauer-derived values (Figure  
339 2b). Supplemental Figure S3a and Table 3 show that high flux centroids are on average  
340 within  $\pm 0.008\text{eV}$  (within  $1\sigma$ ) of low flux centroids. One might conclude from this that the  
341 centroid, as a spectral feature, is a robust proxy for assessment of the  $\text{Fe}^{3+}/\Sigma\text{Fe}$  ratio for  
342 anhydrous glasses. We emphasize again, however, the importance of normalizing to a  
343 standard. While the centroids at the two facilities are reproducible, the individual spectral  
344 features are not. Differences in modelled spectral features (Figures S3b,c,d), and the raw  
345 spectra (Figure S4), reflect the smaller vertical emittance of the 13-ID-E undulator  
346 electron beam compared to the X26A bending magnet source, and the optical

347 configuration at each beamline. That we reproduce the centroids of anhydrous glasses  
348 across facilities to approximately  $\pm 0.01$  eV is a non-trivial result. Fiege et al. (2017) state  
349 that the “overall uncertainty” in the centroid is an order of magnitude higher ( $\pm 0.1$  eV).  
350 We attribute the high precision we achieve primarily to ensuring that we account for  
351 instrumental drift within and between analytical sessions by shifting the energy of all  
352 centroids such that the centroid of LW\_0  $\equiv 7112.3$  eV. The key result is that the  
353 anhydrous glass centroids remain stable within uncertainty at all beam conditions and  
354 across all facilities.

355

356 *Condition XANES<sub>1</sub>, Hydrous Glasses.* At a given  $\text{Fe}^{3+}/\Sigma\text{Fe}$  ratio, the centroids of hydrous  
357 B glasses are variably shifted to higher values at 13-ID-E under nominal operating  
358 conditions (XANES<sub>1</sub>), in stark contrast to the highly reproducible anhydrous glasses  
359 (Table 3). For some hydrous glasses (e.g., B20), we derive the same centroid within  
360 0.003eV (within  $1\sigma$ ) between facilities, but for others (e.g., B11) we derive a centroid up  
361 to 0.25eV higher ( $25\sigma$  higher) under high flux conditions than low flux conditions  
362 (Figure S4). This manifests as XANES-derived  $\text{Fe}^{3+}/\Sigma\text{Fe}$  ratios that are up to 1.7 times  
363 higher than those derived from Mössbauer spectroscopy (Figure 2b).

364

365 *Intensity of 2<sup>nd</sup> Multiplet with Time.* To better evaluate how the Fe XANES spectra of  
366 these glasses evolve with accumulated radiation dose, we conducted experiments to  
367 monitor changes in the intensity of the second pre-edge multiplet at 7113.3 eV (attributed  
368 to  $\text{Fe}^{3+}$ ) as a function of time and flux density (i.e. dose). Glass B11 was used for this  
369 experiment; it is the most hydrous in the suite under study, with 4.82 wt.% total dissolved

370 water. This glass is relatively reduced relative to other hydrous glasses tested, with a  
371  $\text{Fe}^{3+}/\Sigma\text{Fe} = 0.19$ .

372

373 Figure 3 plots the peak amplitude of the second pre-edge multiplet peak of hydrous glass  
374 B11 with time, measured at high flux density and low flux density under both ambient  
375 and cryogenically cooled conditions. We first consider data collected at ambient  
376 temperature. Peak amplitude increases with time under high and low flux conditions, with  
377 a rapid increase observed within the first 100 seconds of high flux irradiation. The higher  
378 photon flux density generated by the focused beam causes a greater increase in the  
379 amplitude of the second pre-edge multiplet at all time points. However, when the change  
380 in amplitude is measured relative to the dose delivered, the amplitude of the second  
381 multiplet (extent of damage) increases at approximately the same rate in high and low  
382 flux density conditions. This evidences the dose-dependence of the spectral change.  
383 While low flux beam damage does not affect the centroid of these hydrous glasses within  
384 the measurement error of our calibration (Figures 2, S5), these data show that damage  
385 occurs in hydrous glasses even at low flux density.

386

387 We then explored the degree to which cryogenic cooling impacts spectral evolution with  
388 time. Studies over a broad range of incident beam energies show that cryo-cooling of  
389 biological samples significantly reduces damage due to mass (water) loss during  
390 exposure to ionizing radiation (e.g. Dubochet et al., 1988; Steinbrecht and Zierold, 2012).  
391 Cryo-cooling may also potentially reduce the rate of beam-induced changes in metal  
392 valence state in some materials (Corbett et al., 2007; Grabolle et al., 2006), although the

393 degree to which this mitigates the effects is debated (Beetz and Jacobsen, 2003; Meents  
394 et al., 2010). We repeated the time series experiments described previously on sample  
395 B11, with the glass held at -195°C. The measurements show the surprising result that at  
396 cryogenic temperatures, under both high and low flux density conditions, the relative rate  
397 of Fe oxidation increases. Beam damage is worse at cryogenic temperatures.

398

399 It is also instructive to see that spectral changes plateau under all conditions studied  
400 within 3-16 minutes. It takes anywhere from approximately 4 to 30 minutes to collect an  
401 entire quality XANES spectrum on glass with FeO concentrations between 5 and 10 wt.%  
402 (e.g. Cottrell and Kelley, 2011; Shorttle et al., 2015). Therefore, successive XANES  
403 spectra, collected at a single sample position, may not show any measurable change if  
404 damage begins to plateau before acquisition of the first spectrum is finished.

405

406 *Conditions XANES<sub>3, 4</sub>. Successive Analysis at one position.* Using glass B11 again, we  
407 show in Figure 4a and Table S3 how the centroids of successive analyses on the same  
408 spot in glass B11 increase if we employ condition XANES<sub>4</sub>, a very low flux achieved by  
409 attenuating and defocusing the beam to 50x50µm. The centroid increases approximately  
410 logarithmically in energy for each successive spectrum. Contrast this with successive  
411 spots at the same incident flux, but with the beam focused to 2x2µm (XANES<sub>3</sub>), in which  
412 case the total number of photons delivered to a given area (photons/µm<sup>2</sup>) is higher after  
413 one spectral acquisition than after successive analyses under condition XANES<sub>4</sub>. The  
414 centroid is commensurately higher, and plateaus after one acquisition. Consistent with  
415 Cottrell et al., 2009, we observe no change in the centroid or pre-edge peak intensities

416 with successive analyses on anhydrous glass AII\_0. Figure 4b reveals how the integrated  
417 intensity (area) of the Gaussian extracted for the first multiplet ( $I_{\text{Fe}^{2+}}$ ) decreases while the  
418 integrated intensity of the second multiplet ( $I_{\text{Fe}^{3+}}$ ) increases. Evolution of the spectra in  
419 this manner is consistent with oxidation of  $\text{Fe}^{2+}$  to  $\text{Fe}^{3+}$ .

420

421 Observations of the raw spectra (Figure 5) confirm the spectral evolution seen in the  
422 modelled parameters. Raw spectra collected sequentially at a given position on sample  
423 B11, under condition XANES<sub>4</sub>, show decreases in the intensity of the first pre-edge  
424 multiplet and increases in intensity of the second pre-edge multiplet. In addition, we see  
425 the main absorption edge move to higher energy as radiation dose accumulates. Spectral  
426 changes are consistent with an increase in the average oxidation state of Fe with  
427 increasing radiation dose.

428

#### 429 *Beam Damage Persists Indefinitely*

430 To assess the longevity of beam damage, we mapped glass B11 approximately one year  
431 after a session in which we investigated beam damage. In figure 6, image brightness  
432 scales with the ratio between the Fe K $\alpha$  fluorescence peak amplitude at 7113.2 eV, the  
433 energy maximum for the  $\text{Fe}^{3+}$  pre-edge multiplet peak, and at 7111.6 eV, the energy  
434 maximum for the  $\text{Fe}^{2+}$  pre-edge multiplet peak. In the false-color inset, the bright white  
435 areas correspond to previously analysed spots. From this map it is evident that areas  
436 exposed to high radiation dose retain higher  $\text{Fe}^{3+}/\text{Fe}^{2+}$  ratios than adjacent areas that were  
437 not exposed to the X-ray beam at least one year after exposure. Beam damage persists  
438 indefinitely.

439

440 *Coordination of Fe in Hydrous and Anhydrous Glasses*

441 Figure 7 compares the summed integrated pre-edge intensities ( $I_{\text{Fe}^{2+}} + I_{\text{Fe}^{3+}}$ ) of hydrous  
442 and anhydrous glasses as a function of their centroids – what Wilke et al. (2001) coined a  
443 “variogram.” A negative non-linear correlation between coordination and oxidation state  
444 is inferred for glasses as well as minerals with mixed geometries (e.g. Jackson et al.,  
445 2005; Wilke et al., 2001). Because  $I_{\text{Fe}^{2+}}$  and  $I_{\text{Fe}^{3+}}$  are extremely sensitive to detector dead  
446 time, edge-step normalization procedure, self-absorption etc., they are generally not  
447 comparable between facilities and are even difficult to compare between analytical  
448 sessions at the same facility (Cottrell et al., 2009). We only compare spectra acquired at  
449 APS in Figure 7; these have been collected and processed under conditions as uniform as  
450 can be practically achieved.

451

452 All glasses display typical pre-edge intensities indicative of 5-fold or mixed 4-fold and 6-  
453 fold coordination (Wilke et al., 2001; Wilke et al., 2005). We see that hydrous glasses fall  
454 along the same trend of increasing integrated pre-edge intensity with centroid energy  
455 under both the high flux density condition XANES<sub>3</sub> and the low flux density condition  
456 XANES<sub>4</sub>. Covariation in the oxidation state and coordination of Fe in these glasses is  
457 consistent with a shift in Fe coordination upon exposure to radiation only in proportion to  
458 the shift in Fe oxidation state. This analysis therefore also points to actual oxidation of  
459  $\text{Fe}^{2+}$  to  $\text{Fe}^{3+}$  in the hydrous glasses.

460

461 The variogram also corroborates the site geometry analysis of the Mössbauer spectra,

462 which revealed higher  $\text{Fe}^{3+}$  isomer shift (and smaller quadrupole splitting) in hydrous B  
463 glasses relative to anhydrous glasses (Figure S1), consistent with longer, weaker, O—  
464  $\text{Fe}^{3+}$  bonds, and  $\text{Fe}^{3+}$  in higher coordination in the hydrous glasses than the anhydrous AII  
465 and LW glasses. In Figure 7, anhydrous glasses display higher integrated intensities  
466 (lower average coordination) than hydrous glasses at any given centroid energy,  
467 consistent with longer and weaker O— $\text{Fe}^{3+}$  bonds in the hydrous glasses. Correcting for  
468 over-absorption does not change this relationship.

469

## 470 **DISCUSSION**

### 471 *Beam Damage Mechanism*

472 The *Is* absorption edge and pre-edge peaks in *3d* transition metals, like Fe, are due to  
473 electron transitions from *Is* to *3d* states (e.g. Henderson et al., 2014). Quadrupole (*Is3d*)  
474 and dipole (*Is* to the *4p* character of the *3d* band) transitions are possible in silicate  
475 glasses, owing to iron's mixed coordination. In XANES spectra,  $\text{Fe}^{2+}$  exhibits 2 or 3 pre-  
476 edge peaks, and  $\text{Fe}^{3+}$  exhibits 1 or 2 pre-edge peaks, depending on coordination (Westre  
477 et al., 1997).  $I_{\text{Fe}^{2+}}$  and  $I_{\text{Fe}^{3+}}$  increase as coordination number decreases (i.e. with higher  
478 extents of *3d* + *4p* mixing) because of the added dipole contribution (Penner-Hahn, 2005;  
479 Roe et al., 1984; Westre et al., 1997). The relative integrated intensities and energies of  
480 the pre-edge peaks therefore depend on the metal site geometry: the relative proportions  
481 of  $\text{Fe}^{2+}$  and  $\text{Fe}^{3+}$  and their coordination as tetrahedral (4-fold) or octahedral (6-fold)  
482 (Henderson et al., 2014; Wilke et al., 2001). Thus, it is necessary to evaluate the degree  
483 to which the observed beam-induced changes in the XANES spectra reflect changes in  
484 effective Fe valence as compared to coordination, particularly since in glasses these

485 effects are coupled.

486

487 We considered the possibility that exposure to radiation in hydrous glasses, but not  
488 anhydrous glasses, might increase  $3d-4p$  hybridization of  $\text{Fe}^{3+}$  centers. For example,  
489  $\text{Fe}^{3+}\text{—OH}^-$  bonds could respond differently to radiation than  $\text{Fe}^{3+}\text{—O}$  bonds. Augmented  
490 hybridization of  $\text{Fe}^{3+}$  centers in hydrous glasses would increase the dipole contribution to  
491 the second multiplet, increase its integrated intensity, and increase the centroid, without  
492 any change in the actual average oxidation state of Fe. Yet, several lines of evidence  
493 argue against this possibility. First, upon exposure to a high photon flux density, the  
494 XANES spectra of the hydrous glasses show that the  $\text{Fe}^{3+}$  multiplet integrated intensity  
495 increases and the  $\text{Fe}^{2+}$  multiplet intensity concomitantly decreases (Figure 4). Moreover,  
496 the white line shifts to progressively higher energy as well (Figure 5). These three  
497 spectral changes together are much more consistent with oxidation of  $\text{Fe}^{2+}$  to  $\text{Fe}^{3+}$  than an  
498 increase in  $3d-4p$  hybridization, as the latter would result in neither a decrease in the  
499 intensity of the first multiplet, nor a shift in the main edge.

500

501 Because no measurable change in the XANES spectra is observed as a function of dose in  
502 spectra collected from anhydrous glasses (e.g. Figures 2, 4), we hypothesize that the  
503 changes we observe in the spectra of hydrous B glasses with exposure to ionizing  
504 radiation relates to their dissolved water contents. Here we use  $\text{Fe}^{3+}/\Sigma\text{Fe}_{\text{Möss}}$  –  
505  $\text{Fe}^{3+}/\Sigma\text{Fe}_{\text{XANES}}$  as a proxy for beam-induced Fe oxidation, where Mössbauer spectra  
506 establish the “true”  $\text{Fe}^{3+}/\Sigma\text{Fe}$  ratio, and the XANES centroid the “apparent”  $\text{Fe}^{3+}/\Sigma\text{Fe}$   
507 ratio (Table 3). Indeed, when we compare glass B8 to B16, glasses of similar  $\text{Fe}^{3+}/\Sigma\text{Fe}$

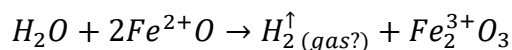
508 ratio, we see that the centroid of glass B16, with > 3.6 times more dissolved water, is  
509 overestimated by ~70%, whereas the centroid of glass B8 is overestimated by ~27%  
510 when exposed to the same radiation dose. Figure 8a shows, however, that total dissolved  
511 H<sub>2</sub>O in the glasses does not correlate with beam-induced Fe oxidation. For example, the  
512 anhydrous XANES calibration of Cottrell et al. (2009) predicts the Fe<sup>3+</sup>/ΣFe ratio of  
513 hydrous glass B17, with 4.67 wt.% total water, within error of its “true” value, while the  
514 centroid of B11, with nearly indistinguishable dissolved water content, is overestimated  
515 by >70% (Figure 4, 11). The latter overestimation of Fe<sup>3+</sup>/ΣFe ratio leads to  
516 overestimation of *f*<sub>O<sub>2</sub></sub> by two orders of magnitude.

517

518 Following this, it is also clear that when the initial oxidation state of Fe is high, the  
519 spectral response to radiation (beam damage) is lessened (Figure 8b). Upon exposure to  
520 the same high photon dose (condition XANES<sub>1</sub>), the Fe<sup>3+</sup>/ΣFe ratios of hydrous glasses  
521 with lower Fe<sup>3+</sup>/ΣFe ratios are greatly overestimated in comparison to glasses with higher  
522 Fe<sup>3+</sup>/ΣFe ratios, which appear to be well predicted by the Mössbauer calibration (R<sup>2</sup>  
523 linear correlation = 0.53; R<sup>2</sup> exponential correlation = 0.72, Figure 8b).

524

525 All the evidence suggests to us that the mechanism of Fe oxidation involves breaking of  
526 O—H bonds by incident ionizing radiation, loss of hydrogen, and concomitant oxidation  
527 of Fe<sup>2+</sup> to Fe<sup>3+</sup>. One possible reaction, analogous to that proposed for radiation-induced  
528 oxidation of S dissolved in hydrous silicate glasses by Klimm et al. (2012) is:



529 The loss of hydrogen gas is consistent with the longevity of the beam damage, as

530 discussed above and shown in Figure 6. This mechanism is also consistent with the  
531 observed dependence on both the initial  $\text{Fe}^{3+}/\Sigma\text{Fe}$  ratio and the dissolved water content of  
532 the hydrous glass.

533

534 The hypothesized mechanism suggests that a fruitful metric for predicting the  
535 susceptibility of hydrous glass to beam damage is the molar ratio of dissolved total water  
536 to the ferric/ferrous ratio as determined by Mössbauer spectroscopy  
537 ( $\Phi = \text{XHO}_{1.5} * \text{XFeO} / \text{XFeO}_{1.5}$  ratio) (Table 1). We find that beam damage susceptibility,  
538  $\Phi$ , correlates strongly with the extent to which high photon flux XANES<sub>1</sub> overestimates  
539 the  $\text{Fe}^{3+}/\Sigma\text{Fe}$  ratio ( $R^2 = 0.92$ ,  $n=14$ ,  $b \equiv 0$  because anhydrous glasses show no damage)  
540 (Figure 8c).

541

542 Inspection of the raw spectra of the B glasses under conditions XANES<sub>3</sub> and XANES<sub>4</sub>  
543 confirms that spectral changes increase as a function of dose and increasing  $\Phi$ , with  
544 anhydrous glasses showing no spectral change (Figure 9). Visual inspection also verifies  
545 that the spectral features all evolve in a manner consistent with oxidation of ferrous iron  
546 to ferric iron:  $I_{\text{Fe}^{2+}}$  falls;  $I_{\text{Fe}^{3+}}$  grows; and the K edge shifts to higher energy. Spectral  
547 changes increase in proportion to  $\Phi$ . We provide the raw spectra for Figure 9 in Table S4.

548

549 We tested this hypothesis by subjecting glass B10 to a 25  $\mu\text{m}$  beam of high photon flux  
550 of  $\sim 1 \times 10^{12}$  photons/sec for  $\sim 12$  minutes (Figure 10). We subsequently mapped the area  
551 surrounding this spot on the sample via Fourier Transform Infrared spectroscopy (FTIR).  
552 The FTIR data show that the area of the glass adjacent to the exposed spot (e.g., pixel 1,

553 Figure 10) also has significantly lower dissolved H<sub>2</sub>O than areas of the glass distant from  
554 exposure (e.g., pixel 2, Figure 10). We reduced individual FTIR spectra from pixels 1 and  
555 2 by fitting the background of the total H<sub>2</sub>O absorption band at 3500 cm<sup>-1</sup> with a spline  
556 function that was then subtracted from the spectra before measuring the band height. This  
557 analysis shows that pixel 2, away from the potential damage zone, has a total dissolved  
558 H<sub>2</sub>O content of 2.43 wt.%, which is identical to the reported H<sub>2</sub>O content for this glass by  
559 Botcharnikov et al. (2005). The dissolved H<sub>2</sub>O content of pixel 1, however, is 900 ppm  
560 lower (2.34 wt.%). Pixel 1 is not coincident with the location of the XANES beam at the  
561 sample surface. Rather, the incident X-ray beam intersects the sample surface at a 45°  
562 angle relative to the FTIR incident beam, which is normal to the sample surface. The high  
563 flux X-ray beam travelled through the sample, from right to left in Figure 10, at 45°  
564 angle, and thus interacted with the glass chip to the left of the beam cross-hair location.  
565 We conclude from this assessment that exposure of this sample to a high-flux XANES  
566 beam caused both oxidation of Fe and loss of H<sub>2</sub>O from the glass, which supports the  
567 proposed mechanism of Fe oxidation via hydrogen loss. We note that only a few percent  
568 of the Fe fluorescence we measure comes from the sample surface. The geometrical  
569 considerations we present above and the magnitude of the spectral changes and water loss  
570 we observe require chemical changes to the bulk affected volume. Damage cannot be  
571 limited to the sample surface.

572

573 Cryo-cooling has been shown to mitigate beam damage (e.g. Steinbrecht and Zierold,  
574 2012; Corbett et al., 2007). Our finding that cryo-cooling exacerbated Fe<sup>2+</sup> oxidation in  
575 hydrous glass is an important and counterintuitive observation. We have shown that

576 hydrogen concentrations in the glass are lower in areas that have experienced oxidizing  
577 beam damage, consistent with radiation-induced breaking of O—H bonds, and  
578 preferential diffusion of hydrogen, relative to oxygen, away from the area. Because it is  
579 the relative diffusivity of hydrogen and oxygen that matters, and diffusivity depends  
580 strongly on temperature, we speculate that oxygen is able to diffuse farther from the  
581 analysed spot in the room temperature case than the cryo-cooled case (whereas hydrogen  
582 is always able to diffuse away). This may be why cryo-cooling is counterproductive  
583 when attempting to mitigate radiation-induced oxidation of Fe in hydrous silicate glass.  
584 Indeed, Gonçalves Ferreira et al. (2013) found that heating soda-lime glasses to 500°C  
585 actually mitigated radiation-induced *reduction* of iron, emphasizing that the effect of  
586 temperature on beam damage will depend on the nature and mechanism of beam damage  
587 and is difficult to predict a priori.

588

## 589 **IMPLICATIONS**

### 590 *Prior XANES studies of hydrous glasses*

591 We have shown that synchrotron radiation causes progressive changes to the XANES  
592 spectra of hydrous glasses, but not anhydrous glasses, as a function of radiation dose.  
593 Spectral changes are consistent with preferential migration of hydrogen relative to  
594 oxygen, and oxidation of iron, in the analysis spot. Our study reveals that oxidative beam  
595 damage occurs in hydrous glasses even at the lowest flux densities achieved, but that  
596 damage is not detectable outside of the error of anhydrous calibrations with exposure to  
597 radiation doses typically found at bending magnet sources. Conversely, it would be  
598 prudent to re-evaluate results from studies carried out on hydrous glasses at undulator

599 beam lines using a focused spot.

600

601 Mafic glasses may be synthesized experimentally with a wide range of  $\Phi$   
602 ( $X\text{HO}_{1.5} * X\text{FeO} / X\text{FeO}_{1.5}$ ) that may readily exceed those investigated in this study. Most  
603 naturally occurring basaltic glasses, however, will have  $0 < \Phi < 1$ . For example, basaltic  
604 glass inclusions in volcanic rocks from subduction zones have  $\Phi$  ranging from  $\sim 0.34$  to  
605  $\sim 1$ ; natural basaltic glasses from sea floor volcanoes erupting in back arc basins have  
606 ratios ranging from  $\sim 0.2$  to  $\sim 0.6$ ; and mid-ocean ridge basalts have ratios between  $\sim 0.05$   
607 to  $\sim 0.28$  (ranges estimated from data in Brounce et al. 2014b; Cottrell and Kelley, 2011;  
608 Kelley and Cottrell, 2012; Zhang et al., submitted). Based on the work presented here, all  
609 submarine basalts and undegassed melt inclusions would suffer significant beam damage  
610 under nominal acquisition conditions (i.e. a focused beam) at unattenuated undulator  
611 beam lines. We have also shown, however, that a radiation dose of  $\leq 6 \times 10^7$   
612 photons/sec/ $\mu\text{m}^2$  mitigates (but does not prevent) beam damage on hydrous glasses with  
613  $\Phi$  up to  $\sim 1$ .

614

615 We hypothesize that previous studies conducted at undulator beam lines have not  
616 detected beam damage in hydrous glasses because, under nominal operating conditions,  
617 radiation damage is maximum or “complete” after acquisition of a single spectrum ( $\sim 600$   
618 seconds for spectra acquired under condition XANES<sub>1</sub>). Collection of multiple spectra at  
619 a single position on the glass under condition XANES<sub>1</sub> will therefore return the same  
620 centroid because damage is complete (“saturated”) before the pre-edge is scanned the  
621 first time (e.g. Moussallam et al., 2016; Moussallam et al., 2014). For materials with

622 relatively low  $\Phi$ , it may be sufficient at an undulator source to attenuate the beam to  
623 prevent beam damage from exceeding detection limits (e.g. Shorttle et al., 2015). We  
624 have shown here, however, that even at the lowest fluxes achievable at 13-ID-E,  
625 attenuation is insufficient to prevent beam damage; the beam must also be defocused.

626

627 *Recommended analytical protocols for acquisition of Fe-XANES spectra on hydrous*  
628 *glasses*

629 Synchrotron radiation causes progressive changes to the XANES spectra of hydrous  
630 glasses as a function of radiation dose and  $\Phi$ . Dose is a function of photon flux, beam  
631 diameter, and exposure time, and can/should be calculated and reported for any  
632 synchrotron experiment. Attenuating the beam, defocusing the spot, or both, may  
633 mitigate beam damage. Using a cryostat is unlikely to mitigate beam damage; it may  
634 even exacerbate damage. This study suggests that a radiation dose of  $\leq 6 \times 10^7$   
635 photons/sec/ $\mu\text{m}^2$  will allow the centroids of most terrestrial basalts to lie within analytical  
636 error of anhydrous calibration curves. We emphasize that beam damage must be assessed  
637 at each beamline and for the specific materials under analysis in a given study.

638

#### 639 **ACKNOWLEDGEMENTS**

640 With admiration, we thank Catherine McCammon, who graciously provided her raw  
641 Mössbauer spectra and laboratory notes to EC. We thank Tim Gooding and Tim Rose for  
642 laboratory support at Smithsonian. EC gratefully acknowledges support from NSF EAR  
643 1347248, NSF EAR 1426717 and NSF OCE 1433212. KK gratefully acknowledges  
644 support from NSF EAR 1347330 and NSF OCE 1433182. We are grateful for support

645 from Smithsonian's Scholarly Studies program. FD also acknowledges support from a  
646 National Museum of Natural History Peter Buck Fellowship. We are grateful for support  
647 for X26A from Department of Energy (DOE) GeoSciences DE-FG02-92ER14244. The  
648 DOE Office of Science supported use of the NSLS under Contract No. DE-AC02-  
649 98CH10886. We acknowledge the support of GeoSoilEnviroCARS (Sector 13), which is  
650 supported by the National Science Foundation - Earth Sciences (EAR-1128799), and the  
651 Department of Energy, Geosciences (DE-FG02-94ER14466). This research used  
652 resources of the Advanced Photon Source, a U.S. Department of Energy (DOE) Office of  
653 Science User Facility operated for the DOE Office of Science by Argonne National  
654 Laboratory under Contract No. DE-AC02-06CH11357. We thank editorial handling by  
655 Sasa Bajt and Keith Putirka as well as two anonymous reviewers for constructive  
656 comments that improved the submission.

657

658

## 659 REFERENCES

- 660 Alberto, H.V., Pinto da Cunha, J.L., Mysen, B.O., Gil, J.M., and Ayres de Campos, N. (1996) Analysis of  
661 Mossbauer spectra of silicate glasses using a two-dimensional Gaussian distribution of hyperfine  
662 parameters. *Journal of Non-Crystalline Solids*, 194, 48-57.
- 663 Arlot, S. and Celisse, A. (2010) A survey of cross-validation procedures for model selection. *Statist.*  
664 *Surv.* 4, 40-79.
- 665 Bajt, S., Sutton, S.R., and Delaney, J.S. (1994) X-Ray Microprobe Analysis of Iron Oxidation-States in  
666 Silicates and Oxides Using X-Ray-Absorption near-Edge Structure (Xanes). *Geochimica Et*  
667 *Cosmochimica Acta*, 58(23), 5209-5214.
- 668 Beetz, T., and Jacobsen, C. (2003) Soft X-ray radiation-damage studies in PMMA using a cryo-STXM.  
669 *Journal of Synchrotron Radiation*, 10(3), 280-283.
- 670 Berry, A.J., O'Neill, H.S.C., Jayasuriya, K.D., Campbell, S.J., and Foran, G.J. (2003) XANES  
671 calibrations for the oxidation state of iron in a silicate glass. *American Mineralogist*, 88(7), 967-  
672 977.
- 673 Botcharnikov, R.E., Koepke, J., Holtz, F., McCammon, C., and Wilke, M. (2005) The effect of water  
674 activity on the oxidation and structural state of Fe in a ferro-basaltic melt. *Geochimica Et*  
675 *Cosmochimica Acta*, 69(21), 5071-5085.
- 676 Brounce, M., Kelley, K., and Cottrell, E. (2014a) Variations in  $Fe^{3+}/\Sigma Fe$  of Mariana arc basalts and  
677 mantle wedge  $fO_2$ . *Journal of Petrology*, 55(12), 2513-2536.
- 678 Brounce, M., Kelley, K.A., and Cottrell, E. (2014b) The  $Fe^{3+}/\Sigma Fe$  variations in Mariana Arc basalts and  
679 primary  $fO_2$  of the mantle wedge. *Journal of Petrology*, 55(12), 2513-2536.
- 680 Carmichael, I.S.E. (1991) The Redox States of Basic and Silicic Magmas - a Reflection of Their Source  
681 Regions. *Contributions to Mineralogy and Petrology*, 106(2), 129-141.
- 682 Corbett, M.C., Latimer, M.J., Poulos, T.L., Sevrioukova, I.F., Hodgson, K.O., and Hedman, B. (2007)  
683 Photoreduction of the active site of the metalloprotein putidaredoxin by synchrotron radiation.  
684 *Acta Crystallographica Section D: Biological Crystallography*, 63(9), 951-960.
- 685 Cottrell, E., and Kelley, K.A. (2011) The oxidation state of Fe in MORB glasses and the oxygen fugacity of  
686 the upper mantle. *Earth and Planetary Science Letters*, 305(3-4), 270-282.
- 687 Cottrell, E., Kelley, K.A., Lanzirotti, A., and Fischer, R.A. (2009) High-precision determination of iron  
688 oxidation state in silicate glasses using XANES. *Chemical Geology*, 268(3-4), 167-179.
- 689 Dixon, J.E., Stolper, E.M., and Holloway, J.R. (1995) An experimental study of water and carbon  
690 dioxide solubilities in mid ocean ridge basaltic liquids .1. Calibration and solubility models.  
691 *Journal of Petrology*, 36(6), 1607-1631.
- 692 Dubochet, J., Adrian, M., Chang, J.-J., Homo, J.-C., Lepault, J., McDowell, A.W., and Schultz, P. (1988)  
693 Cryo-electron microscopy of vitrified specimens. *Quarterly reviews of biophysics*, 21(2), 129-228.
- 694 Dyar, M.D., Breves, E.A., Gunter, M.E., Lanzirotti, A., Tucker, J.M., Carey, C., Peel, S.E., Brown, E.B.,  
695 Oberti, R., and Lerotic, M. (2016) Use of multivariate analysis for synchrotron micro-XANES  
696 analysis of iron valence state in amphiboles. *American Mineralogist*, 101(5), 1171-1189.
- 697 Dyar, M.D., Naney, M.T., and Swanson, S.E. (1987) Effects of Quench Methods on  $Fe^{3+}/Fe^{2+}$  Ratios - a  
698 Mossbauer and Wet-Chemical Study. *American Mineralogist*, 72(7-8), 792-800.
- 699 Eeckhout, S.G., Neisius, T., and Castañeda, C. (2005) Oxidation effects in beryl induced by synchrotron  
700 radiation. *Nuclear Instruments and Methods in Physics Research Section B: Beam Interactions*  
701 *with Materials and Atoms*, 229(1), 73-77.
- 702 Fiege, A., Ruprecht, P., Simon, A.C., Bell, A.S., Göttlicher, J., Newville, M., Lanzirotti, T., and Moore, G.  
703 (2017) Calibration of Fe XANES for high-precision determination of Fe oxidation state in glasses:  
704 Comparison of new and existing results obtained at different synchrotron radiation sources.  
705 *American Mineralogist*, 102(2), 369-380.
- 706 Frost, B.R. (1991) Introduction to oxygen fugacity and its petrologic importance. In D.H. Lindsley, Ed.  
707 *Oxide minerals: Petrologic and magnetic significance*, 25, p. 1-9. BookCrafters Inc., Chelsea, MI.
- 708 Gaetani, G.A., O'Leary, J.A., Shimizu, N., Bucholz, C.E., and Newville, M. (2012) Rapid reequilibration  
709 of  $H_2O$  and oxygen fugacity in olivine-hosted melt inclusions. *Geology*, 40(10), 915-918.

- 710 Gaillard, F., Scaillet, B., Pichavant, M., and Beny, J.L. (2001) The effect of water and fO<sub>2</sub> on the ferric-  
711 ferrous ratio of silicic melts. *Chemical Geology*, 174(1-3), 255-273.
- 712 Grabolle, M., Haumann, M., Müller, C., Liebisch, P., and Dau, H. (2006) Rapid loss of structural motifs in  
713 the manganese complex of oxygenic photosynthesis by X-ray irradiation at 10–300 K. *Journal of*  
714 *Biological Chemistry*, 281(8), 4580-4588.
- 715 Gonçalves Ferreira, P., de Ligny, D., Lazzari, O., Jean, A., Cintora Gonzalez, O., and Neuville, D.R. (2013)  
716 Photoreduction of iron by a synchrotron X-ray beam in low iron content soda-lime silicate glasses.  
717 *Chemical Geology*, 346, 106-112.
- 718 Helz, R., Cottrell, E., Brounce, M., and Kelley, K. (2017) Olivine-melt relationships and syneruptive redox  
719 variations in the 1959 eruption of Kīlauea Volcano as revealed by XANES. *Journal of*  
720 *Volcanology and Geothermal Research*, 333, 1-14.
- 721 Henderson, G.S., de Groot, F.M.F., and Moulton, B.J.A. (2014) X-ray Absorption Near-Edge Structure  
722 (XANES) Spectroscopy. *Reviews in Mineralogy and Geochemistry*, 78(1), 75-138.
- 723 B.L. Henke, E.M. Gullikson, and J.C. Davis. (1993) X-ray interactions: photoabsorption, scattering,  
724 transmission, and reflection at E=50-30000 eV, Z=1-92. *Atomic Data and Nuclear Data Tables*  
725 *Vol. 54 (no.2)*, 181-342.
- 726 Jackson, W.E., F., F., Yeager, M., Mabrouk, P.A., Rossano, S., Waychunas, G.A., Solomon, E.I., and  
727 Brown, G.E. (2005) Multi-spectroscopic study of Fe(II) in silicate glasses: Implications for the  
728 coordination environment of Fe(II) in silicate melts. *Geochimica Et Cosmochimica Acta*, 69,  
729 4315.
- 730 Jayasuriya, K.D., O'Neill, H.S., Berry, A.J., and Campbell, S.J. (2004) A Mossbauer study of the oxidation  
731 state of Fe in silicate melts. *American Mineralogist*, 89(11-12), 1597-1609.
- 732 Johnson, J., Johnson, C., Holland, D., Mekki, A., Appleyard, P., and Thomas, M. (1999) Transition metal  
733 ions in ternary sodium silicate glasses: a Mössbauer and neutron study. *Journal of non-crystalline*  
734 *solids*, 246(1), 104-114.
- 735 Kelley, K.A., and Cottrell, E. (2009) Water and the Oxidation State of Subduction Zone Magmas. *Science*,  
736 325(5940), 605-607.
- 737 -. (2012) The influence of magmatic differentiation on the oxidation state of Fe in a basaltic arc magma.  
738 *Earth and Planetary Science Letters*, 329, 109-121.
- 739 Klimm, K., Kohn, S.C., O'Dell, L.A., Botcharnikov, R.E., and Smith, M.E. (2012) The dissolution  
740 mechanism of sulphur in hydrous silicate melts. I: Assessment of analytical techniques in  
741 determining the sulphur speciation in iron-free to iron-poor glasses. *Chemical Geology*, 322-323,  
742 237-249.
- 743 Kress, V.C., and Carmichael, I.S.E. (1991) The compressibility of silicate liquids containing Fe<sub>2</sub>O<sub>3</sub> and the  
744 effect of composition, temperature, oxygen fugacity and pressure on their redox states.  
745 *Contributions to Mineralogy and Petrology*, 108, 82-92.
- 746 Lagarec, K., and Rancourt, D.G. (1998) RECOIL, Mössbauer spectral analysis software for windows  
747 (version 1.0). Department of Physics, University of Ottawa, Canada.
- 748 Lagarec, K., and Rancourt, D. (1997) Extended Voigt-based analytic lineshape method for determining N-  
749 dimensional correlated hyperfine parameter distributions in Mössbauer spectroscopy. *Nuclear*  
750 *Instruments and Methods in Physics Research Section B: Beam Interactions with Materials and*  
751 *Atoms*, 129(2), 266-280.
- 752 Le Voyer, M., Cottrell, E., Kelley, K.A., Brounce, M., and Hauri, E.H. (2015) The effect of primary versus  
753 secondary processes on the volatile content of MORB glasses: An example from the equatorial  
754 Mid- Atlantic Ridge (5° N–3° S). *Journal of Geophysical Research: Solid Earth*, 120(1), 125-144.
- 755 Matjuschkin, V., Brooker, R.A., Tattitch, B., Blundy, J.D., and Stamper, C.C. (2015) Control and  
756 monitoring of oxygen fugacity in piston cylinder experiments. *Contributions to Mineralogy and*  
757 *Petrology*, 169(1), 1-16.
- 758 Meents, A., Gutmann, S., Wagner, A., and Schulze-Briese, C. (2010) Origin and temperature dependence  
759 of radiation damage in biological samples at cryogenic temperatures. *Proceedings of the National*  
760 *Academy of Sciences*, 107(3), 1094-1099.
- 761 Moor, J., Fischer, T., Sharp, Z., King, P., Wilke, M., Botcharnikov, R., Cottrell, E., Zelenski, M., Marty,  
762 B., and Klimm, K. (2013) Sulfur degassing at Erta Ale (Ethiopia) and Masaya (Nicaragua)

- 763 volcanoes: Implications for degassing processes and oxygen fugacities of basaltic systems.  
764 *Geochemistry, Geophysics, Geosystems*, 14(10), 4076-4108.
- 765 Moore, G., Righter, K., and Carmichael, I.S.E. (1995) The Effect of Dissolved Water on the Oxidation-  
766 State of Iron in Natural Silicate Liquids. *Contributions to Mineralogy and Petrology*, 120(2), 170-  
767 179.
- 768 Moussallam, Y., Edmonds, M., Scaillet, B., Peters, N., Gennaro, E., Sides, I., and Oppenheimer, C. (2016)  
769 The impact of degassing on the oxidation state of basaltic magmas: A case study of Kīlauea  
770 volcano. *Earth and Planetary Science Letters*, 450, 317-325.
- 771 Moussallam, Y., Oppenheimer, C., Scaillet, B., Gaillard, F., Kyle, P., Peters, N., Hartley, M., Berlo, K., and  
772 Donovan, A. (2014) Tracking the changing oxidation state of Erebus magmas, from mantle to  
773 surface, driven by magma ascent and degassing. *Earth and Planetary Science Letters*, 393, 200-  
774 209.
- 775 Mysen, B.O., Carmichael, I.S.E., and Virgo, D. (1985a) A Comparison of Iron Redox Ratios in Silicate-  
776 Glasses Determined by Wet-Chemical and Fe-57 Mossbauer Resonant Absorption Methods.  
777 *Contributions to Mineralogy and Petrology*, 90(2-3), 101-106.
- 778 Mysen, B.O., and Richet, P. (2005) *Silicate Glasses and Melts - Properties and Structure*. 548 p. Elsevier,  
779 New York.
- 780 Mysen, B.O., and Virgo, D. (1989) Redox equilibria, structure, and properties of Fe-bearing  
781 aluminosilicate melts: Relationships between temperature, composition, and oxygen fugacity in the  
782 system Na<sub>2</sub>O-Al<sub>2</sub>O<sub>3</sub>-SiO<sub>2</sub>-FeO. *American Mineralogist*, 74, 58-76.
- 783 Mysen, B.O., Virgo, D., Neumann, E.R., and Seifert, F.A. (1985b) Redox Equilibria and the Structural  
784 States of Ferric and Ferrous Iron in Melts in the System CaO-MgO-Al<sub>2</sub>O<sub>3</sub>-SiO<sub>2</sub>-FeO -  
785 Relationships between Redox Equilibria, Melt Structure and Liquidus Phase-Equilibria. *American*  
786 *Mineralogist*, 70(3-4), 317-331.
- 787 Penner-Hahn, J.E. (2005) X-ray Absorption Spectroscopy.
- 788 Roe, A., Schneider, D., Mayer, R., Pyrz, J., Widom, J., and Que Jr, L. (1984) X-ray absorption  
789 spectroscopy of iron-tyrosinate proteins. *Journal of the American Chemical Society*, 106(6), 1676-  
790 1681.
- 791 Rowe, M.C., Kent, A.J.R., and Nielsen, R.L. (2007) Determination of sulfur speciation and oxidation state  
792 of olivine hosted melt inclusions. *Chemical Geology*, 236(3-4), 303-322.
- 793 Sack, R.O., Carmichael, I.S.E., Rivers, M., and Ghiorso, M.S. (1980) Ferric-Ferrous Equilibria in Natural  
794 Silicate Liquids at 1bar. *Contributions to Mineralogy and Petrology*, 75(4), 369-376.
- 795 Shimizugawa, J., Umesaki, M., Hanada, M., Sakai, M., and Qiu, M. (2001) X-ray induced reduction of rare  
796 earth ion doped in Na<sub>2</sub>O-Al<sub>2</sub>O<sub>3</sub>-B<sub>2</sub>O<sub>3</sub> glasses. *Journal of synchrotron radiation*, 8(2), 797-799.
- 797 Shorttle, O., Moussallam, Y., Hartley, M.E., MacLennan, J., Edmonds, M., and Murton, B.J. (2015) Fe-  
798 XANES analyses of Reykjanes Ridge basalts: Implications for oceanic crust's role in the solid  
799 Earth oxygen cycle. *Earth and Planetary Science Letters*, 427, 272-285.
- 800 Stamper, C., Melekhova, E., Blundy, J., Arculus, R., Humphreys, M., and Brooker, R. (2014) Oxidised  
801 phase relations of a primitive basalt from Grenada, Lesser Antilles. *Contributions to Mineralogy*  
802 *and Petrology*, 167(1), 954.
- 803 Steinbrecht, R.A., and Zierold, K. (2012) *Cryotechniques in biological electron microscopy*. Springer  
804 Science & Business Media.
- 805 Sutton, S.R., Lanzirotti, A., Newville, M., Rivers, M.L., Eng, P., and Leticariu, L. (2017) Spatially  
806 Resolved Elemental Analysis, Spectroscopy and Diffraction at the GSECARS Sector at the  
807 Advanced Photon Source. *Journal of Environment Quality*, 0(0), 0.
- 808 Tappero, R., Smith, R.J., Acerbo, A.S., DiFabio, J., and Miller, L. (2016) Can cryo-cooling mitigate  
809 chemical changes for hydrated samples? *International Conference on X-ray Microscopy*.
- 810 Tappero, R., Smith, R.J., Acerbo, A.S., Lanzirotti, A., Newville, M., Sutton, S.R., Northrup, P., O'Hara, S.,  
811 and Miller, L.M. (2017) A portable cryostage system for X-ray fluorescence microprobes. 14th  
812 *International Conference on the Biogeochemistry of Trace Elements (ICOBTE)*.
- 813 Westre, T.A., Kennepohl, P., DeWitt, J.G., Hedman, B., Hodgson, K.O., and Solomon, E.I. (1997) A  
814 Multiplet Analysis of Fe K-Edge 1s-3d Pre-Edge Features of Iron Complexes. *Journal of*  
815 *American Chemical Society*, 119, 6297-6314.

- 816 Wilke, M., Behrens, H., Burkhard, D.J.M., and Rossano, S. (2002) The oxidation state of iron in silicic  
817 melt at 500 MPa water pressure. *Chemical Geology*, 189(1-2), 55-67.
- 818 Wilke, M., Farges, F., Petit, P.-E., Brown, G.E., Jr., and Martin, F. (2001) Oxidation state and coordination  
819 of Fe in minerals: An Fe K-XANES spectroscopic study. *American Mineralogist*, 86(5-6), 714-  
820 730.
- 821 Wilke, M., Jugo, P.J., Klimm, K., Susini, J., Botcharnikov, R., Kohn, S.C., and Janousch, M. (2008) The  
822 origin of S<sup>4+</sup> detected in silicate glasses by XANES. *American Mineralogist*, 93(1), 235-240.
- 823 Wilke, M., Partzsch, G.M., Bernhardt, R., and Lattard, D. (2005) Determination of the iron oxidation state  
824 in basaltic glasses using XANES at the K-edge. *Chemical Geology*, 220(1-2), 143-161.
- 825 Wilke, M., Schmidt, C., Farges, F., Malavergne, V., Gautron, L., Simionovici, A., Hahn, M., and Petit, P.E.  
826 (2006) Structural environment of iron in hydrous aluminosilicate glass and melt-evidence from X-  
827 ray absorption spectroscopy. *Chemical Geology*, 229(1-3), 144-161.
- 828 Zhang, H.L., Cottrell, E., Hirschmann, M.M., and Kelley, K.A. (submitted) Determination of Fe<sup>3+</sup>/ΣFe of  
829 XANES basaltic glass standards by Mössbauer spectroscopy and its application to the oxidation  
830 state of iron in MORB. *Chemical Geology*.
- 831 Zhang, H.L., Hirschmann, M.M., Cottrell, E., Newville, M., and Lanzirrotti, A. (2016) Structural  
832 environment of iron and accurate determination of Fe<sup>3+</sup>/ΣFe ratios in andesitic glasses by XANES  
833 and Mössbauer spectroscopy. *Chemical Geology*, 428, 48-58.
- 834 Zhang, H.L., Solheid, P.A., Lange, R.A., von der Handt, A., and Hirschmann, M.M. (2015) Accurate  
835 determination of Fe<sup>3+</sup>/ΣFe of andesitic glass by Mössbauer spectroscopy. *American Mineralogist*,  
836 100(8-9), 1967-1977.

837  
838  
839  
840 **FIGURE CAPTIONS**

841

842 **Figure 1.** XANES spectra for hydrous B glasses and anhydrous LW and AII glasses  
843 under three radiation dose conditions. Left hand panels show full spectra; right hand  
844 panels magnify the pre-edge region. Spectra are color-coded by relative Fe<sup>3+</sup>/ΣFe ratio as  
845 determined by Mössbauer spectroscopy (black are the most reduced glasses, grading  
846 through red and orange to yellow, which are the most oxidized glasses). Note the  
847 smooth, monotonic, decrease in the intensity in the first pre-edge multiplet and increase  
848 in intensity of the second pre-edge multiplet as a function of Fe<sup>3+</sup>/ΣFe ratio for the  
849 hydrous samples under the bending magnet and low radiation dose conditions, and the  
850 anhydrous glasses under all dose conditions. Spectra of hydrous B glasses under the high  
851 radiation dose condition do not evolve systematically as a function of Fe<sup>3+</sup>/ΣFe ratio.

852

853 **Figure 2. (A)**  $\text{Fe}^{3+}/\Sigma\text{Fe}$  ratios determined by Mössbauer spectroscopy versus  $\text{Fe}^{3+}/\Sigma\text{Fe}$   
854 ratios determined by XANES at a flux of  $10^{6-7}$  photons/sec/ $\mu\text{m}^2$  using the anhydrous  
855 basalt calibration curve of Cottrell et al. (2009). Filled circles: anhydrous basalts, Cottrell  
856 et al. (2009). Open squares: hydrous basalts, Botcharnikov et al (2005). Filled squares  
857 and filled triangles: hydrous basalts, this study. The anhydrous basalts, on which this  
858 calibration is based, fall slightly off the 1:1 line because we have used the average  
859 centroid of these glasses collected over a 10 year period (n=30-50 per glass) as reported  
860 in Zhang et al. (submitted) to highlight the reproducibility of the measurement. **(B)** The  
861 same analysis as in (A), but at a higher flux of  $10^{10}$  photons/sec/ $\mu\text{m}^2$ . Vertical  $1\sigma$  error  
862 bars are smaller than the symbol sizes. Horizontal  $1\sigma$  error bars are the errors on the  
863 Mössbauer determinations. Dashed lines show the predictive capability of the model  
864 using a leave-one-out cross validation method (Arlot and Celisse, 2010). The root mean  
865 square uncertainty for the predicted  $\text{Fe}^{3+}/\Sigma\text{Fe}$  ratios of unknowns determined from the  
866 basaltic calibration is  $<\pm 0.01$  ( $1\sigma$ ).

867

868 **Figure 3.** Time-dependence of the intensity of the second pre-edge multiplet ( $\Delta\text{FeK}\alpha/\text{IO}$ )  
869 during exposure to synchrotron radiation under four beam conditions: high flux density  
870 (filled squares) and low flux density (open circles); and at ambient temperature (red) and  
871 with the sample cryogenically cooled to  $-195^\circ\text{C}$  (blue). The intensity of the second pre-  
872 edge multiplet is higher (i.e. more radiation-induced oxidative beam damage) when the  
873 sample is cryogenically cooled under both beam conditions.

874

875 **Figure 4.** Evolution of spectral features as a function of spectrum number (proxy for

876 dose) for spectra acquired in succession in the same position on the sample for hydrous  
877 glass B11 and anhydrous glass AII. **(A)** Evolution of centroids under two beam  
878 conditions, high radiation dose condition XANES<sub>3</sub> ('+' and 'x' symbols) and low  
879 radiation dose condition XANES<sub>4</sub> (circles and triangles). Centroids of successive spots on  
880 anhydrous glass AII show no significant changes under either beam condition.

881 Application of a high radiation dose, typical of focused beams at undulator beamlines,  
882 does not result in significant changes to the centroids of successive spectra on the same  
883 spot of hydrous glass B11; however, centroids acquired using a high radiation dose are  
884 higher than centroids collected on the same sample at low radiation dose. Significant  
885 increases in the centroids of successive spots on hydrous glass B11 only become apparent  
886 using a low radiation dose. Vertical 1 $\sigma$  error bars are smaller than the symbol sizes.

887 **(B)** Evolution of I<sub>Fe2+</sub> and I<sub>Fe3+</sub> with successive spectra taken at the same position under  
888 low radiation dose condition XANES<sub>4</sub>. Vertical 1 $\sigma$  error bars are smaller than the symbol  
889 sizes.

890

891 **Figure 5. (A)** Evolution the background-subtracted pre-edge, acquired via successive  
892 analyses in the same sample position, as a function of radiation dose, using condition  
893 XANES<sub>4</sub>. As the total dose increases, the intensity of the first pre-edge multiplet  
894 decreases while the second increases. **(B)** The main edge moves to progressively higher  
895 energy as dose increases.

896

897 **Figure 6.** The grey-scale image is a peak amplitude map collected at ~7113.2 eV (energy  
898 of 2nd pre-edge multiplet) of hydrous glass B11. Image color is scaled to maximum

899 intensity, where white is high and black is low. The inset map is a peak amplitude map  
900 collected at 7113.2/7111.6eV (peak amplitude of the 2nd pre-edge multiplet divided by  
901 the peak amplitude of the 1st pre-edge multiplet). Image color is scaled to maximum peak  
902 amplitude, where white is high and red is low. White areas show spots analysed >1 year  
903 earlier.

904

905 **Figure 7.** A “variogram” showing the spectral characteristics of centroid versus  
906 integrated pre-edge intensity (area) of Fe in end-member structural environments (large  
907 empty circles) from Wilke et al., 2001 and glasses from this study. Anhydrous (black  
908 circles) and hydrous glass (red and blue squares) spectral characteristics from this study  
909 are consistent with iron in five-fold coordination or a mixture of four-fold and six-fold  
910 coordination. Under the same radiation dose conditions, anhydrous glasses display higher  
911 pre-edge intensities relative to hydrous glasses at a given centroid energy. Hydrous  
912 glasses under high radiation dose conditions display higher pre-edge intensities than  
913 under low radiation dose conditions; however, increases in pre-edge intensities are  
914 proportional to increases in the centroid ( $\text{Fe}^{3+}/\Sigma\text{Fe}$  ratio). Vertical  $1\sigma$  error bars are  
915 smaller than the symbol sizes.

916

917 **Figure 8.** We use  $\Phi = \text{Fe}^{3+}/\Sigma\text{Fe}_{\text{Möss}} - \text{Fe}^{3+}/\Sigma\text{Fe}_{\text{XANES}}$  as a proxy for beam-induced Fe  
918 oxidation (where Mössbauer spectra establish the “true”  $\text{Fe}^{3+}/\Sigma\text{Fe}$  ratio, and the XANES  
919 centroid the “apparent”  $\text{Fe}^{3+}/\Sigma\text{Fe}$  ratio). The molar concentration of **(A)** dissolved water  
920 (single cation basis),  $\text{XHO}_{1.5}$ , **(B)** ferric iron (single cation basis),  $\text{XFeO}_{1.5}$ , and **(C)** the  
921 ratio of dissolved water multiplied by the ferrous/ferric ratio,  $\text{XHO}_{1.5} * \text{XFeO}/\text{XFeO}_{1.5}$ ,

922 versus  $\%Fe^{3+}/\Sigma Fe_{Möss} - Fe^{3+}/\Sigma Fe_{XANES}$ . The correlation in (C) is forced through the  
923 origin, because we observe no oxidative beam damage in anhydrous glasses.  $1\sigma$  error  
924 bars are smaller than the symbol sizes.

925

926 **Figure 9.** Pre-edge spectra of one anhydrous and four hydrous glasses, with varying  $\Phi$   
927 and under two radiation dose conditions. We display merged, successive spectra,  
928 acquired under two different beam conditions: high radiation dose condition XANES<sub>3</sub>  
929 (red) and low radiation dose condition XANES<sub>4</sub> (blue). The black line shows the  
930 difference between the spectra.

931

932 **Figure 10. (A)** FTIR transmission map of glass B10 surrounding an area purposely  
933 exposed with a  $2 \times 2 \mu m$  synchrotron radiation beam at a photon flux of  $\sim 1 \times 10^{12}$   
934 photons/sec for  $\sim 12$  minutes. We show the location of the beam at the sample surface, but  
935 the beam intersects the sample surface at a  $45^\circ$  angle and travels through the sample from  
936 left to right. Color scale shows the intensity of the  $H_2O_{Total}$  absorbance band at  $3500 \text{ cm}^{-1}$   
937 after subtraction of a reference intensity at  $2300 \text{ cm}^{-1}$ . Each pixel is  $20 \times 20 \mu m$ . FTIR  
938 spectra for pixels designated (1) and (2) are discussed in the text.

939

Table 1: Room Temperature Mössbauer hyperfine parameters, Fe<sup>3+</sup>/ΣFe ratios, and select compositional parameters

Sample	Fe <sup>3+</sup> /ΣFe * 100				spectral fitting parameters (this study)										B et al., 2005		Φ <sup>^</sup>
	B et al. 2005	1σ	this study	1σ	χ <sup>2</sup>	Bkgrd.	Fe <sup>3+</sup> CS	Fe <sup>3+</sup> δCS	Fe <sup>3+</sup> QS	Fe <sup>3+</sup> δQS	Fe <sup>2+</sup> CS	Fe <sup>2+</sup> δCS	Fe <sup>2+</sup> QS	Fe <sup>2+</sup> δQS	FeO Total Wt.%	H2O Total Wt.%	
B11	19	2	18.7	1.45	1.0	1024543	0.46	0.19	0.93	0.14	0.95	0.12	1.98	0.44	12.49	4.82	1.05
B16	18	2	16.8	1.23	0.8	1427668	0.53	0.09	0.92	0.39	0.95	0.14	1.97	0.41	12.93	3.02	0.81
B12	11	2	12.3	1.81	1.2	598904	0.52	0.28	1.12	0.01	0.97	0.14	2.00	0.42	12.02	1.9	0.77
B13	10	2	12	1.41	1.0	1988275	0.48	0.34	1.00	0.02	0.94	0.03	1.91	0.48	11.39	1.71	0.72
B10	40	4	36.3	1.61	1.1	680688	0.50	0.02	0.90	0.38	0.91	0.28	2.02	0.12	12.61	2.43	0.24
B6	39	3	36.9	1.72	1.2	644411	0.44	0.02	0.91	0.46	0.96	0.12	1.93	0.38	12.94	2	0.19
B9	29	3	26.7	2.14	1.4	570588	0.55	0.19	0.82	0.00	0.91	0.28	1.99	0.10	12.62	1.14	0.19
B7	23	2	21.1	0.94	0.6	1068960	0.57	0.18	0.87	0.00	0.92	0.28	1.94	0.12	12.91	0.97	0.22
B8	16	2	17.8	1.15	0.8	905216	0.59	0.02	0.92	0.34	0.93	0.28	1.92	0.14	12.67	0.82	0.23
B17	60	2	55.6	2.03	1.4	392639	0.50	0.16	0.88	0.29	0.93	0.29	2.11	0.09	12.65	4.67	0.19
B21	49	2	45.7	1.58	1.1	735417	0.50	0.05	0.90	0.38	0.89	0.31	2.04	0.15	12.34	2.9	0.19
B19	52	2	49.3	1.68	1.1	628828	0.54	0.15	0.82	0.28	0.81	0.28	2.21	0.11	12.91	1.85	0.11
B22	28	2	25.3	0.38	0.3	5545128	0.58	0.20	0.82	0.00	0.89	0.28	1.98	0.11	12.77	0.94	0.17
B20	25	2	24.8	1.00	0.7	2254268	0.58	0.20	0.83	0.00	0.90	0.28	1.98	0.11	12.80	0.72	0.13
			C et al., 2009 <sup>v</sup>	1σ	χ <sup>2</sup>	Bkgrd.	Fe <sup>3+</sup> CS	Fe <sup>3+</sup> δCS	Fe <sup>3+</sup> QS	Fe <sup>3+</sup> δQS	Fe <sup>2+</sup> CS	Fe <sup>2+</sup> δCS	Fe <sup>2+</sup> QS	Fe <sup>2+</sup> δQS			
All_0	-	-	14.7	0.38	0.55	5408375	0.44	0.09	1.31	0.47	0.95	0.15	1.88	0.44	-	-	-
All_05	-	-	19.4	0.63	0.63	7463896	0.50	0.17	1.27	0.46	0.95	0.16	1.88	0.42	-	-	-
All_-05	-	-	13.8	0.50	0.5	6400103	0.44	0.04	1.30	0.63	0.95	0.18	1.88	0.37	-	-	-
All_15	-	-	24.7	0.44	0.44	5948886	0.44	0.03	1.26	0.50	0.95	0.17	1.88	0.42	-	-	-
All_-15	-	-	9.3	0.60	0.6	694310	0.44	0.33	1.29	0.03	0.95	0.14	1.88	0.45	-	-	-
All_25	-	-	35.6	0.38	0.38	5951129	0.41	0.09	1.27	0.50	0.95	0.18	1.88	0.41	-	-	-
All_35	-	-	48.4	0.40	0.4	12486195	0.38	0.10	1.25	0.48	0.93	0.17	1.88	0.14	-	-	-
All_45	-	-	61.1	0.26	0.26	10318722	0.37	0.09	1.26	0.48	0.91	0.18	1.88	0.44	-	-	-
LW_0	-	-	16.2	0.55	0.38	7123408	0.44	0.14	1.23	0.55	0.95	0.16	1.90	0.42	-	-	-
LW_10	-	-	23.5	0.53	0.53	7922396	0.46	0.17	1.22	0.40	0.95	0.15	1.91	0.43	-	-	-
LW_-10	-	-	13.0	0.58	0.58	9201577	0.44	0.10	1.25	0.70	0.95	0.16	1.90	0.42	-	-	-
LW_20	-	-	30.3	0.14	1.4	2072205	0.30	0.12	1.22	0.48	0.86	0.10	1.91	0.47	-	-	-
LW_-20	-	-	8.8	0.53	0.53	6835643	0.44	0.03	1.28	0.03	0.95	0.15	1.90	0.42	-	-	-

<sup>v</sup> Cottrell et al., 2009. Recommended Fe<sup>3+</sup>/ΣFe ratios, considering recoilless fraction, can be found in Zhang et al., submitted. Room Temperature values are used in this work for comparison with Botcharnikov et al., 2005.

<sup>^</sup> Φ = XH<sub>0.5</sub>\*XFeO/XFeO<sub>1.5</sub> based on Fe<sup>3+</sup>/ΣFe ratios from this study and H<sub>2</sub>O from Botcharnikov et al., 2005.

940

Table 2: Synchrotron radiation dose conditions

Flux Condition	spot size (μm)	photon flux (photons/sec)	flux density (photons/sec/μm <sup>2</sup> )	Gray/sec**	notes
XANES <sub>1</sub>	2x2	5 x 10 <sup>10-11</sup>	1x10 <sup>10-11</sup>	9.0x10 <sup>10-11</sup>	nominal at 13-ID-D
XANES <sub>3</sub>	2x2	1.5-8.6 x 10 <sup>9</sup>	4 x10 <sup>8</sup> to 2 x10 <sup>9</sup>	~1.3x10 <sup>7</sup>	
XANES <sub>4</sub>	50x50	1.5-8.6 x 10 <sup>9</sup>	8 x10 <sup>5</sup> to 3 x10 <sup>6</sup>	~1.3x10 <sup>4</sup>	
XANES <sub>5</sub>	25x25	2 x 10 <sup>9</sup>	3x10 <sup>6</sup>	3.8x10 <sup>4</sup>	
XANES <sub>CRYO-HI</sub>	38x28	3-4 x 10 <sup>7</sup>	3-4 x 10 <sup>4</sup>		monochrometer = 7113.3eV
XANES <sub>CRYO-LO</sub>	38x28	2-4 x 10 <sup>6</sup>	2-4 x 10 <sup>3</sup>		monochrometer = 7113.3eV
X26A	9x5	3 x10 <sup>9</sup>	6x10 <sup>7</sup>	7.7x10 <sup>5</sup>	

\*\*Dose in Gray (Joules/kg/sec) is calculated for glass of basaltic composition through 1/e absorption length

Table 3: XANES centroids and integrated pre-edge intensities

sample	X26A♦				XANES <sub>1</sub>				XANES <sub>5</sub>				
	5x10 <sup>10</sup> photons/um <sup>2</sup>				3x10 <sup>15</sup> photons/um <sup>2</sup>				2x10 <sup>9</sup> photons/um <sup>2</sup>				
	centroid	σ	I1	I2	centroid	σ	I1	I2	centroid	σ	I1	I2	%Δ**
B11	7112.402	0.012	0.06	0.037	7112.654	0.015	0.053	0.066	7112.421	0.003	0.058	0.045	71.9
B16	7112.342	0.008	0.063	0.031	7112.578	0.007	0.057	0.057	7112.362	0.01	0.061	0.04	69.2
B12	7112.226	0.007	0.073	0.026	7112.4	0.016	0.07	0.046	7112.228	0.002	0.074	0.032	66.4
B13	7112.177	0.002	0.077	0.024	7112.328	0.011	0.073	0.038	7112.211	0.015	0.076	0.031	46.0
B10	7112.784	0.01	0.047	0.062	7112.86	0.018	0.045	0.082	7112.773	0.004	0.048	0.074	18.4
B6	7112.733	0.012	0.05	0.06	7112.793	0.017	0.049	0.076	7112.735	0.007	0.052	0.07	6.5
B9	7112.585	0.006	0.06	0.05	7112.633	0.006	0.06	0.066	7112.568	0.011	0.06	0.058	16.5
B7	7112.477	0.007	0.064	0.042	7112.505	0.009	0.066	0.054	7112.468	0.009	0.064	0.05	18.7
B8	7112.413	0.007	0.07	0.04	7112.451	0.026	0.066	0.05	7112.418	0.006	0.067	0.047	27.2
B17	7113.083	0.013	0.03	0.088	7113.108	0.016	0.029	0.106	7113.059	0.001	0.032	0.098	3.8
B21	7112.988	0.006	0.039	0.082	7113.029	0.014	0.039	0.104	7112.957	0.008	0.04	0.088	15.5
B19	7113.01	0.008	0.04	0.083	7112.99	0.011	0.042	0.097	7112.969	0.008	0.042	0.094	2.3
B22	7112.587	0.01	0.062	0.051	7112.613	0.008	0.06	0.064	7112.582	0.01	0.06	0.06	19.1
B20	7112.548	0.002	0.064	0.048	7112.551	0.009	0.064	0.058	7112.538	0.009	0.063	0.057	9.5
	5x10 <sup>10</sup> photons/um <sup>2</sup>				4x10 <sup>15</sup> photons/um <sup>2</sup>								
All0	7112.275	0.01	0.091	0.03	7112.271	0.009	0.079	0.036					
All05	7112.361	0.011	0.086	0.038	7112.368	0.002	0.08	0.046					
All-05	7112.219	0.01	0.09	0.029	7112.22	0.004	0.084	0.034					
All15	7112.52	0.013	0.078	0.047	7112.529	0.002	0.069	0.058					
All-15	7112.147	0.026	0.093	0.02	7112.134	0.007	0.087	0.025					
All25	7112.742	0.014	0.068	0.07	7112.76	0.009	0.061	0.079					
All35	7112.962	0.027	0.055	0.091	7112.974	0.002	0.052	0.106					
All45	7113.184	0.025	0.046	0.124	7113.186	0.003	0.042	0.14					
LW_0	7112.3	0.01	0.085	0.032	7112.302	0.01	0.079	0.04					
LW10	7112.434	0.013	0.078	0.042	7112.433	0.009	0.07	0.05					
LW-10	7112.154	0.024	0.095	0.023	7112.155	0.004	0.085	0.028					
LW20	7112.608	0.02	0.072	0.058	7112.62	0.002	0.069	0.069					
LW-20	7112.112	0.01	0.097	0.018	7112.128	0.002	0.092	0.027					

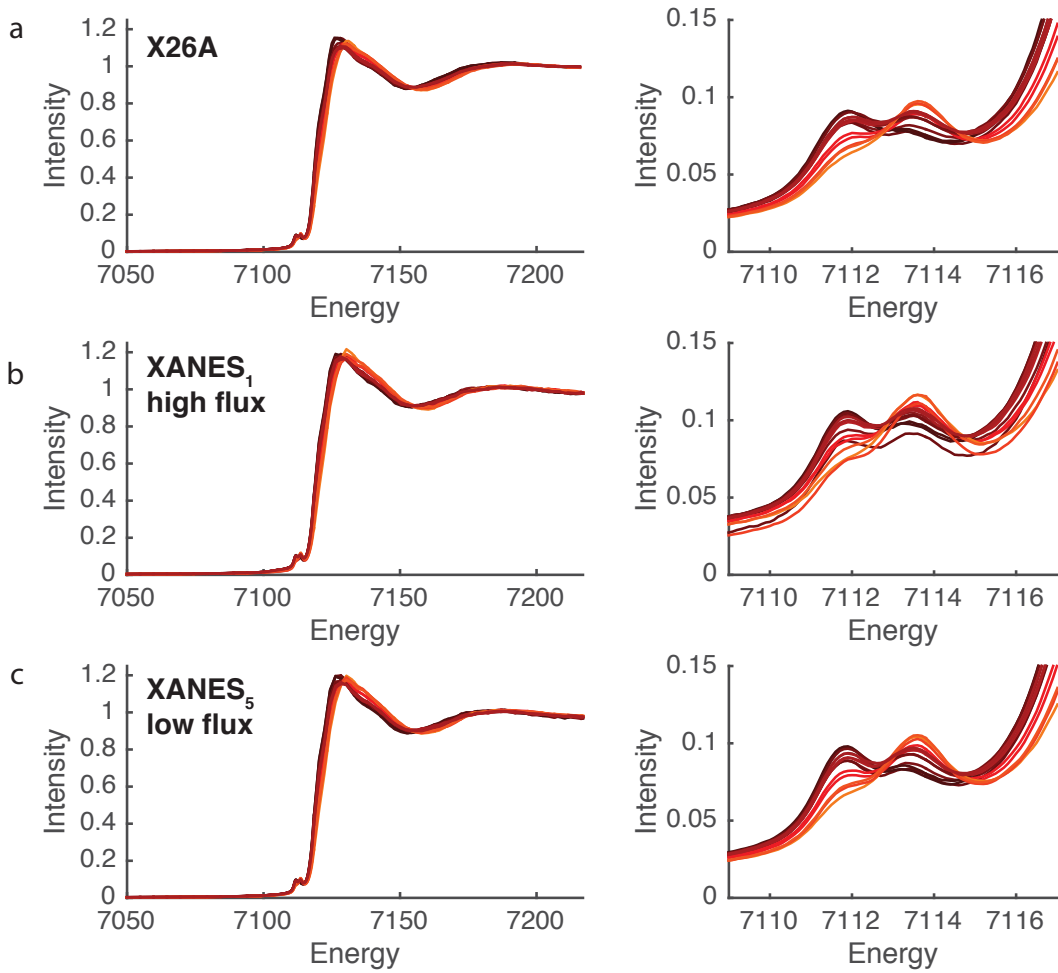
♦ centroids are 7-yr avgs (n=30-48) as reported in Zhang et al., submitted

\*\* $\text{Fe}^{3+}/\Sigma\text{Fe}_{\text{Möss}} - \text{Fe}^{3+}/\Sigma\text{Fe}_{\text{XANES}}$

Doses reported in this table are per spectrum (photons/sec/μm<sup>2</sup>\*total collection time)



### Hydrous B Glasses



### Anhydrous LW and All Glasses

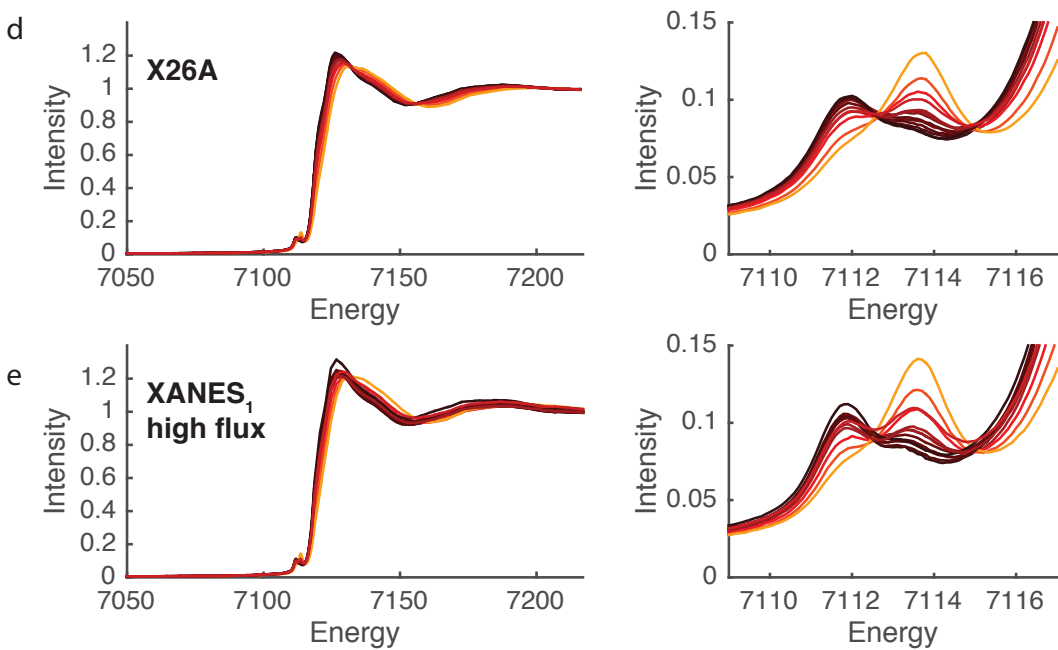


Figure 1

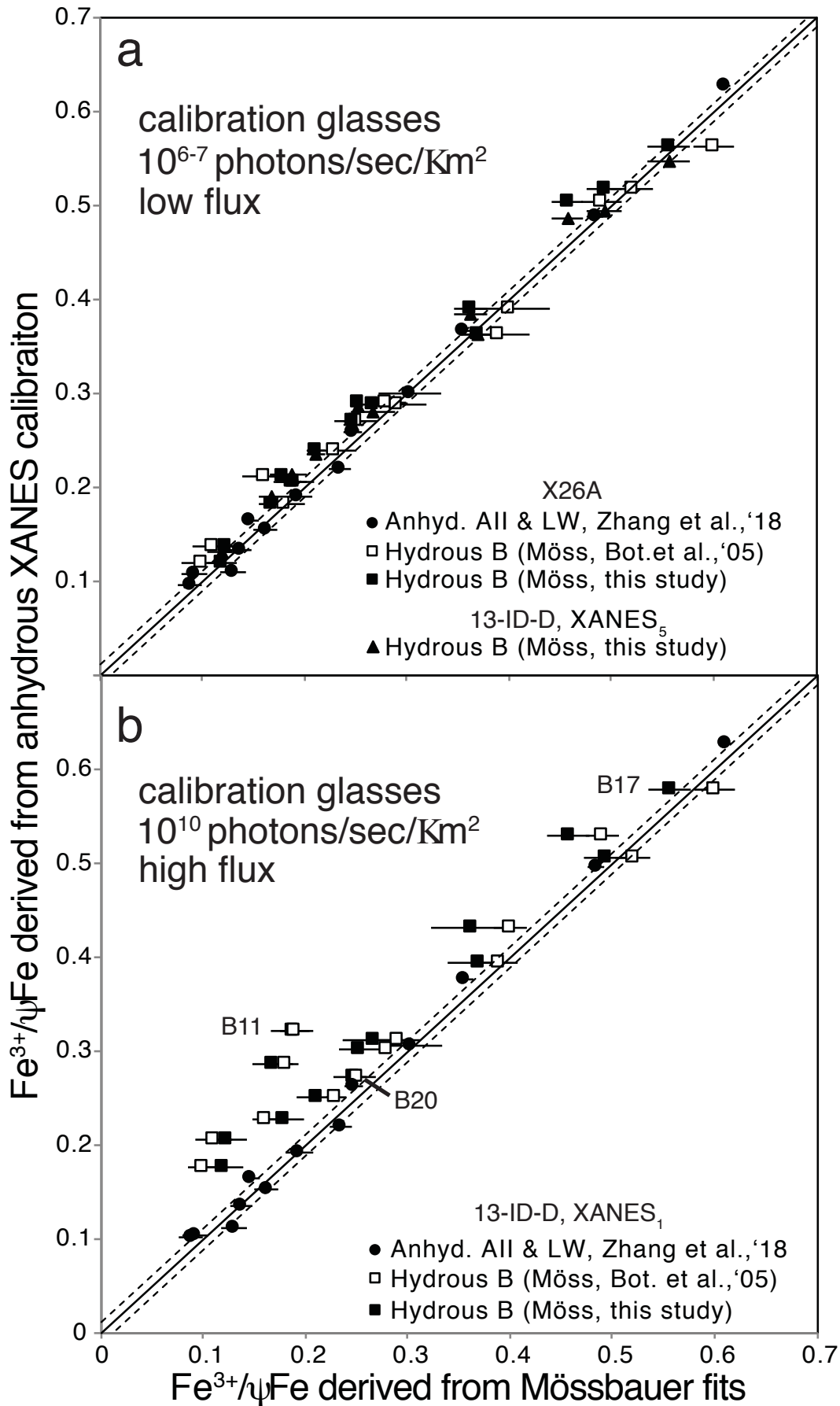


Figure 2

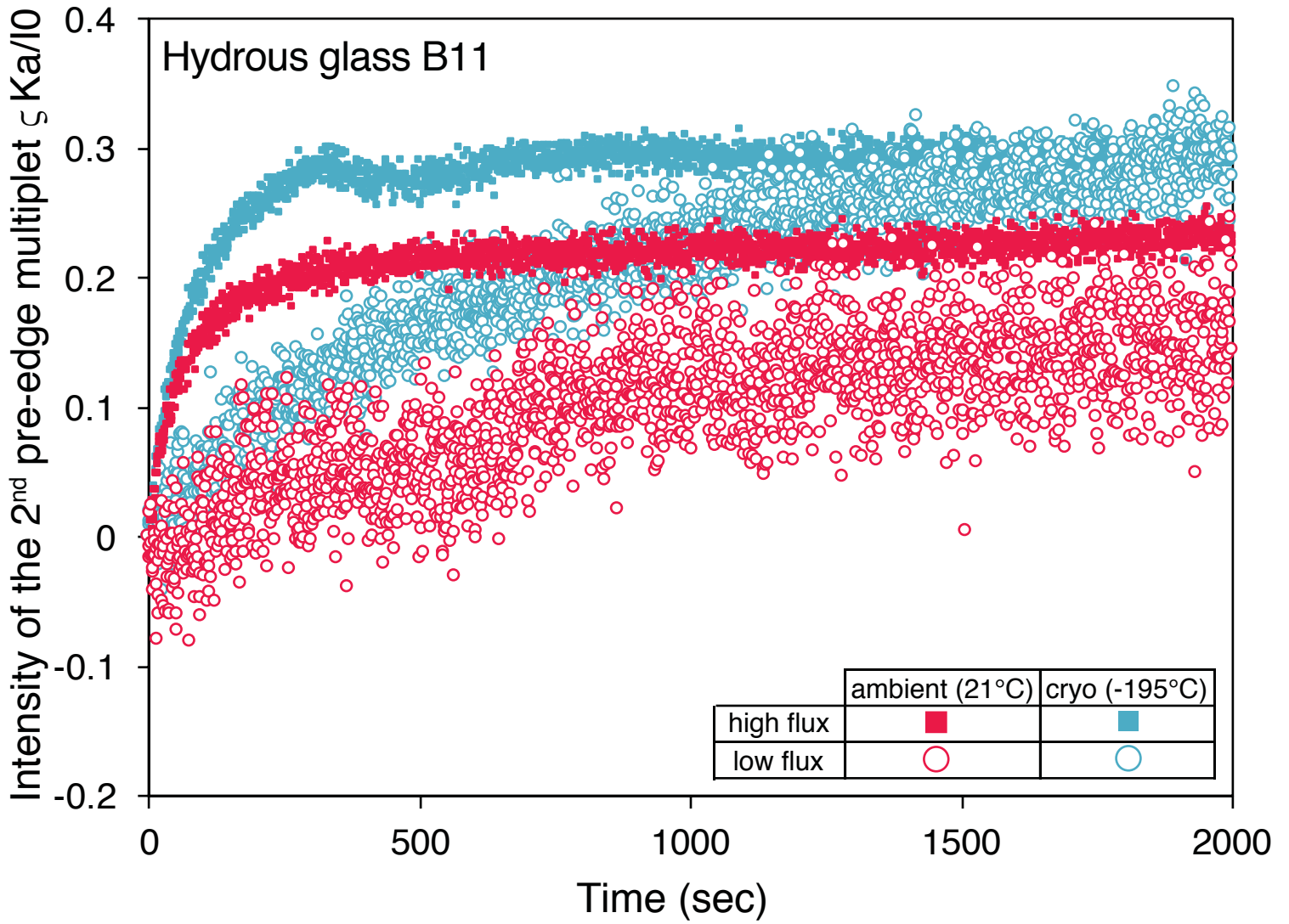


Figure 3

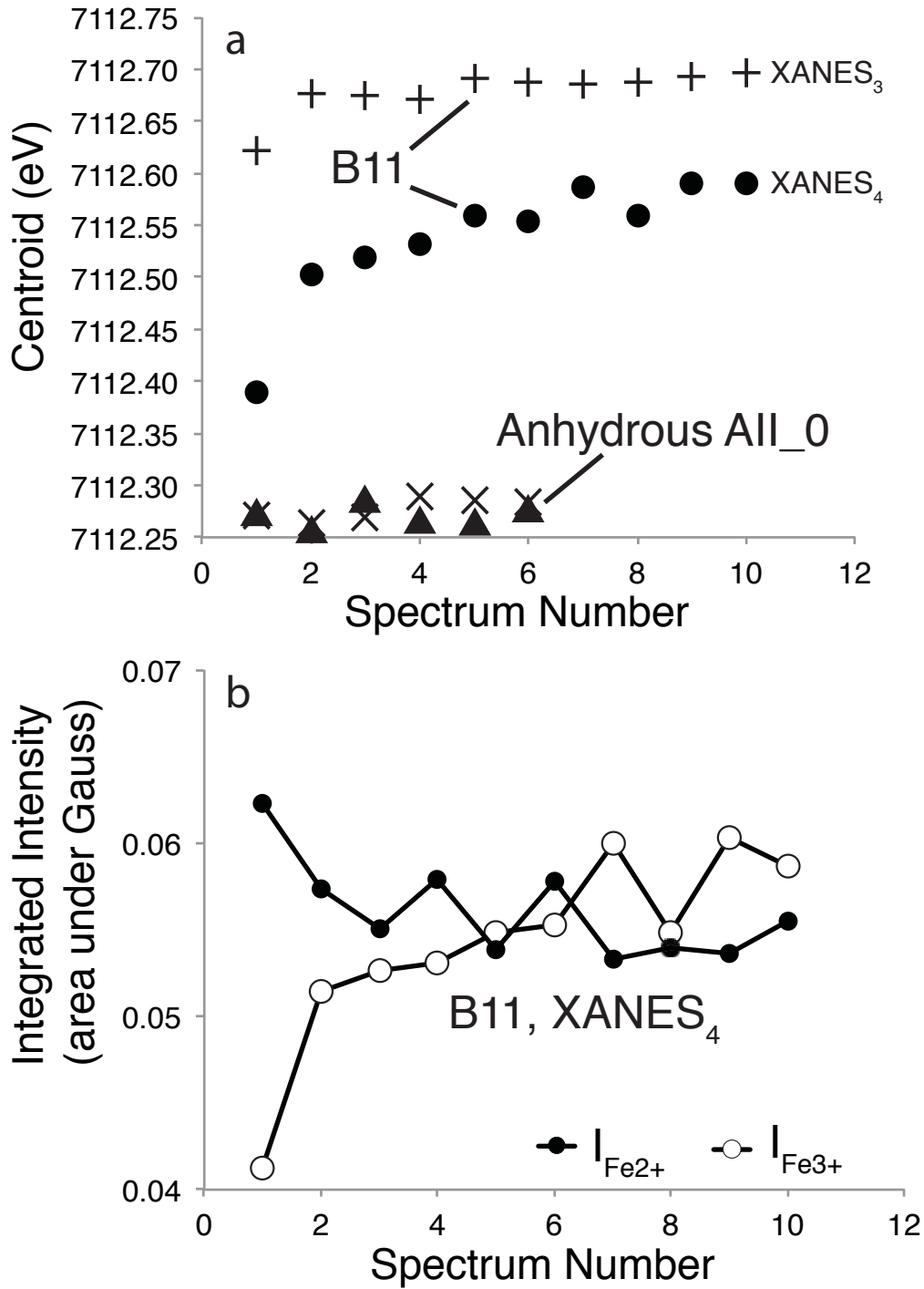


Figure 4

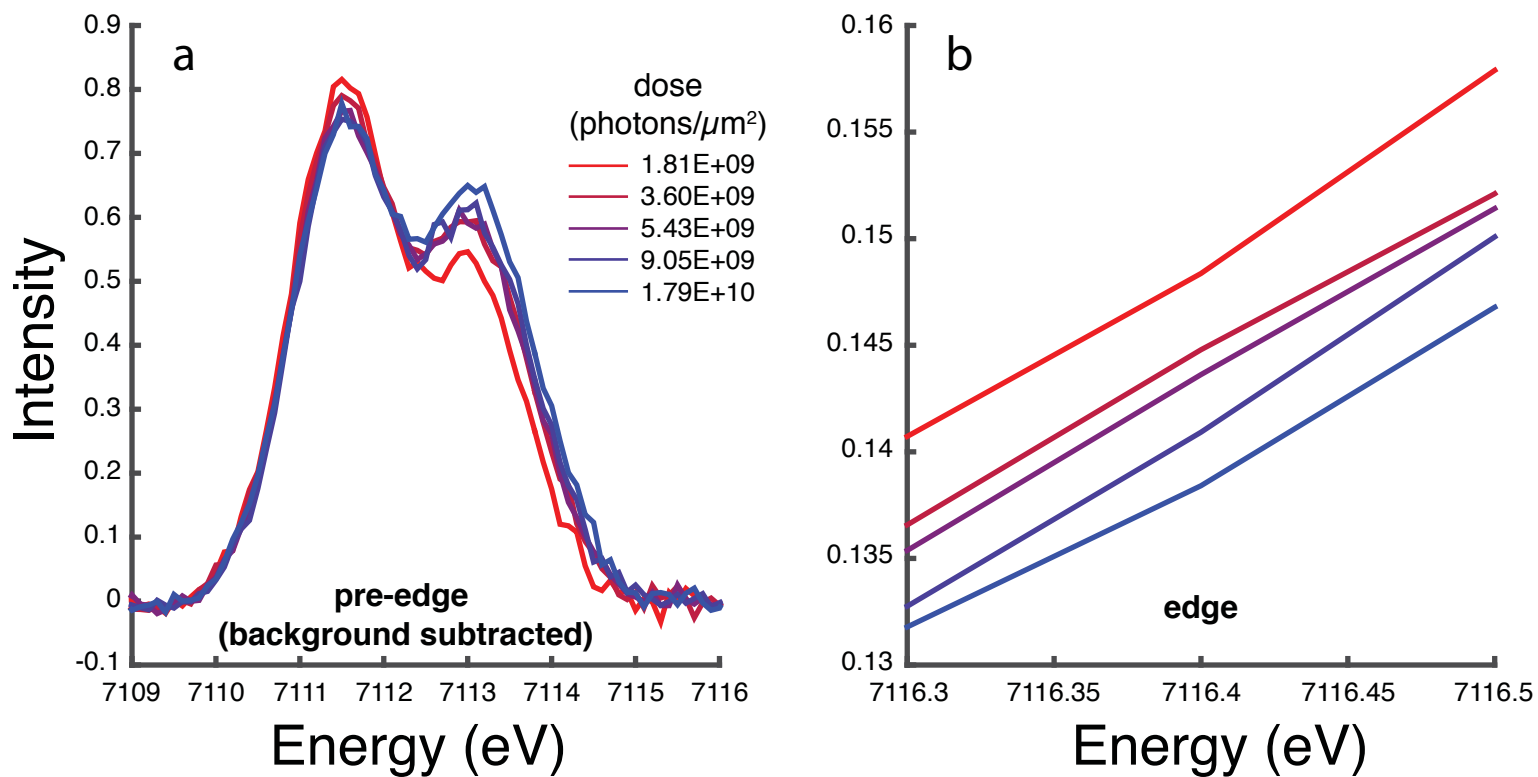


Figure 5

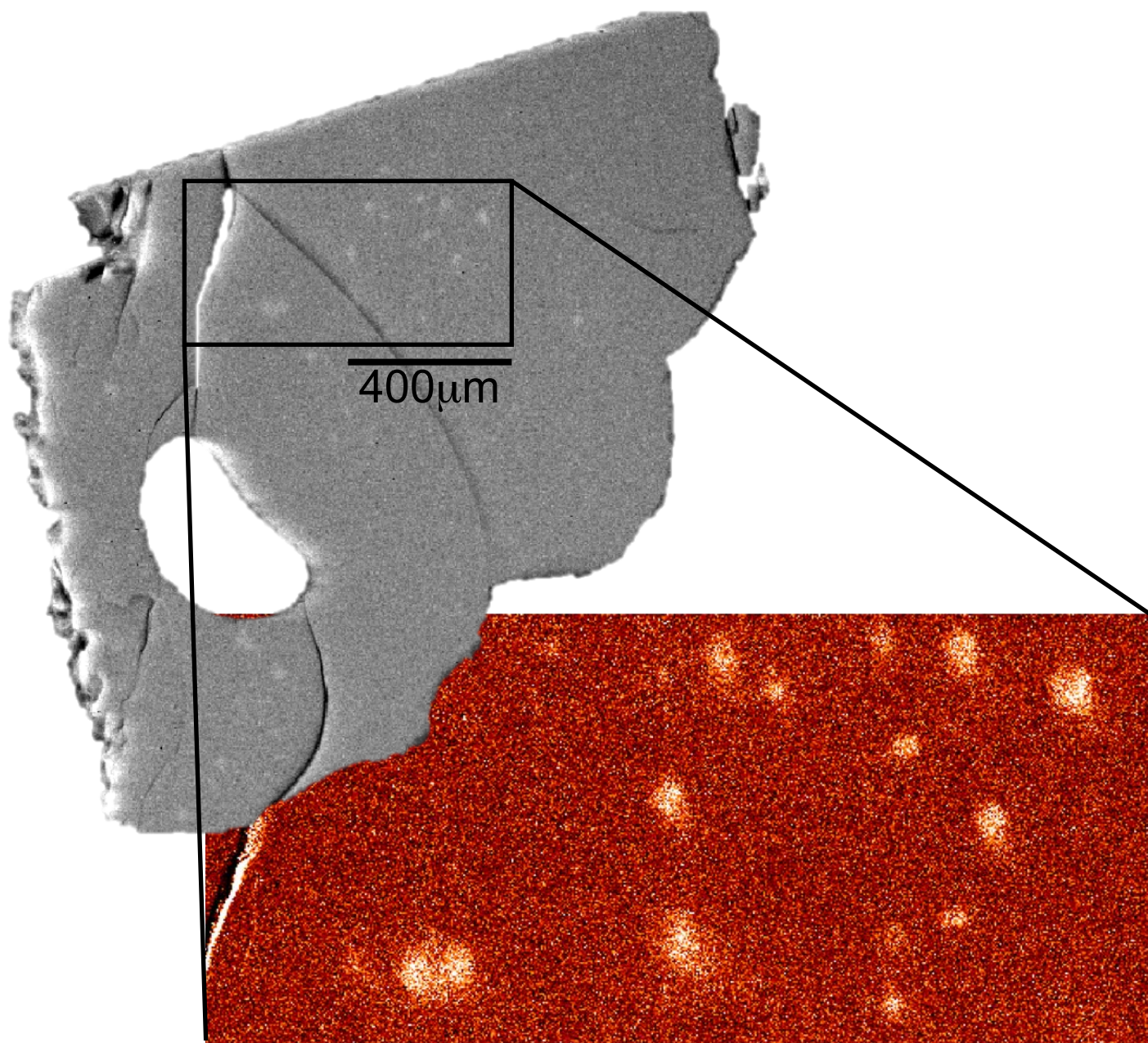


Figure 6

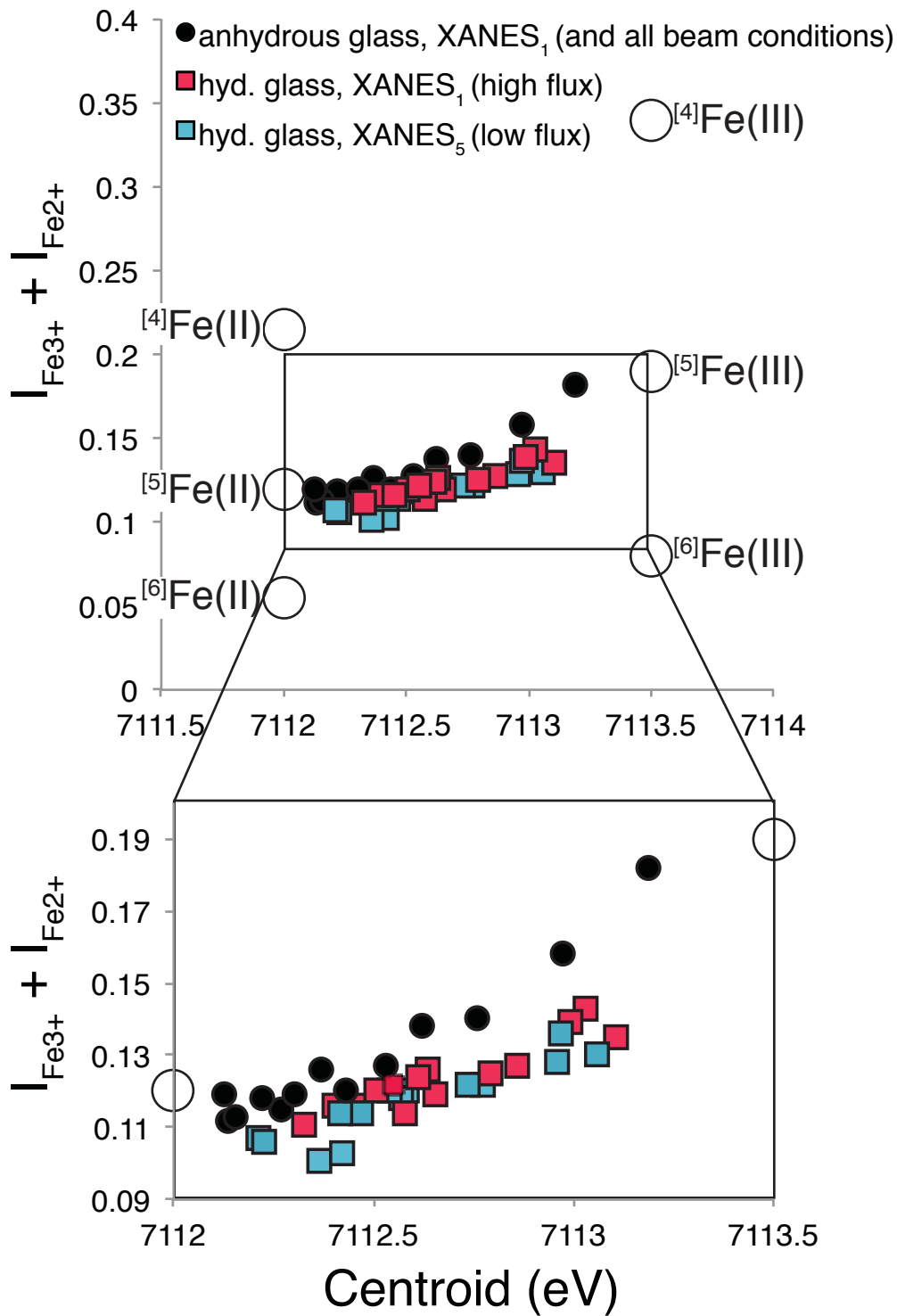


Figure 7

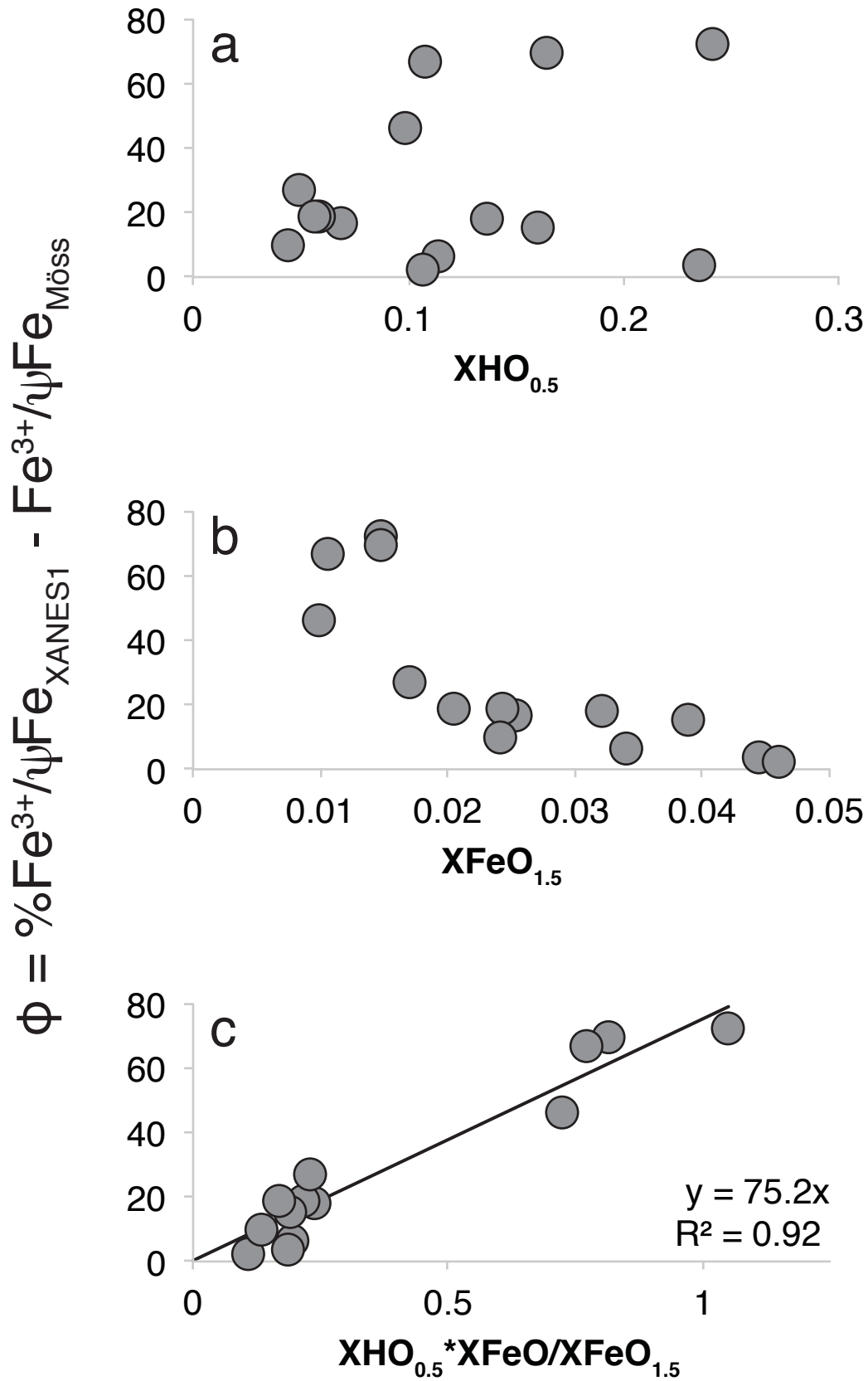


Figure 8

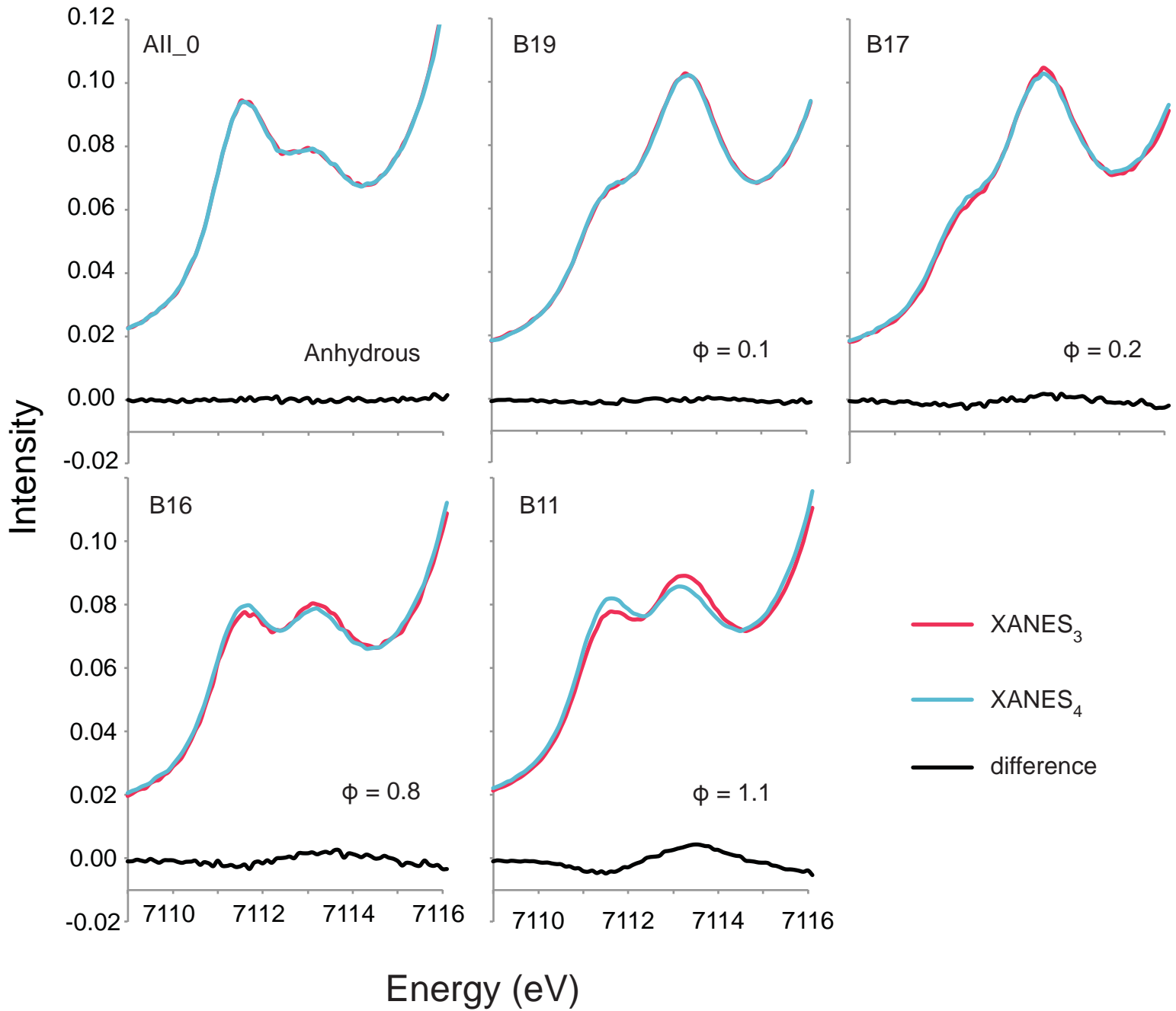


Figure 9

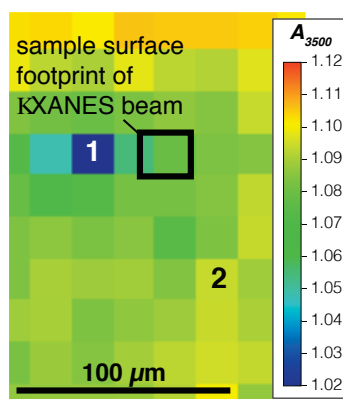


Figure 10